TECHNISCHE UNIVERSITÄT WIEN
Vienna University of Technology

Dosimetric comparison of manual and automatic AI-assisted registration for assessment of interfraction variations in MR-guided adaptive brachytherapy.

Diplomarbeit

zur Erlangung des akademischen Grades

Diplom-Ingenieur

im Rahmen des Studiums

Biomedical Engineering

an der Fakultät für Physik der TU Wien eingereicht von

Christian Wöbke, B.Sc. **11930508**

betreut durch

Betreuer	Univ.-Prof. Dr. DI Dietmar Georg
In Zusammenarbeit mit	Assoc. Prof. Mag. Dr. Nicole Eder-Nesvacil und Stefan Ecker, PhD

Wien, 17. Mai 2024

Christian Wöbke Dietmar Georg

TECHNISCHE UNIVERSITÄT WIEN
Vienna University of Technology

Dosimetric comparison of manual and automatic AI-assisted registration for assessment of interfraction variations in MR-guided adaptive brachytherapy.

Diploma thesis

submitted for partial fulfillment of the requirements for the degree of

Diplom-Ingenieur

in

Biomedical Engineering

to the Faculty of Physics at TU Wien, authored by

Christian Wöbke, B.Sc. **11930508**

supervised by

Advisor	Univ.-Prof. Dr. DI Dietmar Georg
Assistance	Assoc. Prof. Mag. Dr. Nicole Eder-Nesvacil
	Stefan Ecker, PhD

Vienna, May 17, 2024

Christian Wöbke Dietmar Georg

ACKNOWLEDGEMENTS

I would like to take this opportunity to thank the people who have supported and guided me through this thesis. First and foremost, I would like to thank Univ.-Prof. Dr. DI Dietmar Georg for supervising me and making this thesis possible. Special thanks also go to Assoc. Prof. Dr. Nicole Eder-Nesvacil and Stefan Ecker, PhD, for their excellent practical and scientific support.

I'm also grateful to the brachytherapy team of the Department of Radiation Oncology at the Vienna General Hospital (AKH)/ Medical University Vienna (MUW) for their willingness to answer all my clinical questions and introduce me to the clinical procedures. I would like to thank Dr. Vincent Moritz Dick for the contouring of the organ at risk (OAR).

I'd like to acknowledge my parents, my girlfriend Kitten, and my friends, who have always motivated me. Finally, I would like to thank all those who have proofread this thesis (special thanks to Theresia and Nette)

ERKLÄRUNG ZUR VERFASSUNG DER ARBEIT

Christian Wöbke, B.Sc.

Hiermit erkläre ich, dass es sich bei der vorliegenden Arbeit um meine eigene Arbeit handelt. Alle Stellen, die wörtlich oder sinngemäß aus veröffentlichten Quellen entnommen wurden, sind als solche kenntlich gemacht. Diese Arbeit wurde weder in gleicher noch ähnlicher Form bisher keinem anderen Prüfungsausschuss vorgelegt und wurde nicht veröffentlicht.

Vienna, May 17, 2024

Christian Wöbke

ABSTRACT

The standard treatment for locally advanced cervical cancer is external beam radiotherapy followed by a brachytherapy boost. This method leads to excellent clinical results. At the Department of Radiation Oncology of the Vienna General Hospital/ MedUni Vienna, such a boost is typically administered in four fractions of high-dose rate (HDR) brachytherapy. From a clinical point of view, organ motion between fractions has been shown to be within acceptable ranges for most patients. Therefore, the same treatment plan can be used for two consecutive days of treatment. However, some patients present with significant organ motion. These cases require intervention of the planning team. The process of assessing interfraction variations is currently performed either visually or by landmark-based rigid image registration, which is a manual and time-consuming process, and therefore difficult to implement in clinical practice. Currently there are no solutions for rapid quantitative evaluation of organ at risk interfraction motion in commercial treatment planning systems (TPS). Novel deep learning methods based on convolutional neural networks have shown great promise to overcome this challenge. A detailed comparison between the dosimetric impact of both methods is still pending. The aim of this thesis is to quantitatively assess the difference between standard manual TPS-based applicator registration and novel artificial intelligence (AI) - based method by analyzing the dosimetric impact of registration uncertainties for both methods. To achieve this goal, a test cohort of 9 female cervical cancer patients (N=9) underwent a repetitive imaging protocol during treatment. These image sets were registered for each subject using both the conventional manual method (which served as a benchmark) and the algorithm supported by AI. The impact of registration uncertainties was evaluated via discrete dose volume histogram parameters of organs at risk. The results of this study show that there are differences in how organs at risk are affected by existing registration uncertainties of the AI-based registration method. For bladder and sigmoid, the dosimetric impact of the registration uncertainties is more pronounced than for bowel and rectum. The analysis of inter- and intrafraction motion highlighted the importance of integrating a fully automated assessment workflow in the future. This study underscores the promising role of AI in enhancing brachytherapy treatment planning, suggesting further research into its integration could significantly improve clinical outcomes for patients with cervical cancer and reduce the workload for the cervical cancer treatment.

KURZFASSUNG

Die Standardbehandlung für lokal fortgeschrittenen Gebärmutterhalskrebs ist die Teletherapie gefolgt von einer Brachytherapie. Diese Kombination hat ausgezeichnete klinische Ergebnisse gezeigt. In der Universitätsklinik für Radioonkologie des Allgemeinen Krankenhaus in Wien wird die Brachytherapie in der Regel in vier Fraktionen der Hochdosis-Brachytherapie aufgeteilt. Zwischen den Fraktionen kann es zu Organbewegungen kommen, die jedoch bei den meisten Patienten in einem klinisch nicht relevanten Bereich liegen. Aus diesem Grund kann der gleiche Behandlungsplan an zwei aufeinander folgenden Behandlungstagen angewendet werden. Bei einigen Patienten können jedoch Organbewegungen auftreten, die zu klinisch relevanten Veränderungen führen. In diesen Fällen muss das Planungsteam eingreifen. Die Beurteilung von Interfraktionsvariationen erfolgt derzeit entweder visuell oder durch eine starre Bildregistrierung auf der Basis von Applikator-basierten „landmarks“. Dies ist jedoch ein zeitaufwändiger Prozess und daher schwer in den klinischen Alltag zu integrieren. Eine schnelle quantitative Bewertung der Interfraktionsverschiebungen von Risikoorganen ist daher in kommerziellen Behandlungsplanungssystemen derzeit nur eingeschränkt möglich. Neue Deep-Learning-Methoden auf der Basis Gefalteter Neuronaler Netze haben sich als vielversprechend erwiesen, um dieser Herausforderung zu begegnen. Bisher fehlte jedoch eine detaillierte Untersuchung des dosimetrischen Einflusses der Rekonstruktionsabweichung der künstlichen Intelligenz (KI) basierten Methoden. Ziel dieser Arbeit war es daher, den Unterschied zwischen der standardmäßigen manuellen Applikator-Registrierung im Planungssystem und einer neuen AI-basierten Methode quantitativ zu bewerten, indem die dosimetrischen Auswirkungen der Registrierungsunsicherheiten für beide Methoden analysiert und verglichen werden. Um dieses Ziel zu erreichen, wurde eine Testkohorte von 9 Probandinnen (N=9) während der Behandlung einem wiederholten Bildgebungsprotokoll unterzogen. Diese Bilder wurden für jede Testperson sowohl mit der herkömmlichen manuellen Methode (die als Referenz diente) als auch mit dem KI-unterstützten Algorithmus registriert. Die Auswirkungen der Registrierunsicherheiten wurden mit Hilfe von diskreten Dosis-Volumen-Histogramm - Parametern der Risikoorgane bewertet. Durch die Ergebnisse dieser Studie konnte gezeigt werden, wie die Risikoorganen durch bestehende Registrierungsunsicherheiten der KI-basierten Registrierungsmethode beeinflusst werden. Der dosimetrische Einfluss durch die Registrierungsunsicherheit ist für die Blase und beim Sigmoid stärker ausgeprägt als im Darm und Rektum. Die Analyse der inter- und intrafraktionellen Bewegung zeigte, wie wichtig es ist, in Zukunft einen vollständig automatisierten Auswerteprozess zu integrieren. Diese Studie unterstreicht die vielversprechende Rolle der KI bei der Verbesserung der Brachytherapie-Behandlungsplanung und deutet darauf hin, dass weitere Forschungsarbeiten zu ihrer Integration in die Behandlung die klinischen Ergebnisse für Patienten mit Zervixkarzinom und auch die Effizienz der Arbeitsabläufe erheblich verbessern könnten.

LIST OF ABBREVIATIONS

3D	three dimensional
AI	artificial intelligence
AKH	Vienna General Hospital
AS	applicator structure
BT	brachytherapy
CT	computed tomography
CTV-T$_{IR}$	clinical intermediate-risk target volume
CTV-T$_{HR}$	clinical high-risk target volume
CTV-T$_{LR}$	clinical low-risk target volume
DICOM	Digital Imaging and Communications in Medicine
DVH	dose volume histogram
EBRT	external beam radiotherapy
EQD2	equieffective absorbed dose
FIGO	International Federation of Gynecology and Obstetrics
GTV	gross tumor volume
HDR	high-dose rate
HPV	Human Papilloma Virus
IGABT	image-guided adaptive brachytherapy
IQR	interquartile range
LACC	locally advanced cervical cancer

LDR	low-dose rate
MR	magnetic resonance
MDR	intermediate-dose rate
Max	maximum
M	mean
MDE	mean distance error
MUW	Medical University Vienna
Med	median
Min	minimum
OAR	organ at risk
PDR	pulse-dose rate
SD	random uncertainties/standard deviation
TPS	treatment planning systems

LIST OF FIGURES

LIST OF TABLES

TABLE OF CONTENTS

1. INTRODUCTION

Cervix Cancer is the fourth most common type of cancer that affects women, globally. In 2020, the number of new cases was estimated at about 604 000 (3.1 %) and the number of deaths at about 342 000 (3.4 % of the total cancer cases worldwide) [1] .Today, cervical cancer can be prevented quite well, especially in highly developed areas of the world [2]. The most common prevention methods are the human papilloma virus (HPV) vaccination and screening. Approximately 90% of all cases of cervical cancer occur in low- and middle-income countries without organized screening and HPV vaccination programs. In high-income countries, cervical cancer incidence and mortality being reduced by more than 50% during the last 30 years since the introduction of formal screening programs [3]. There are still many patients who need treatment. The treatment of cervical cancer involves multidisciplinary methods and depends on the size and spread of the tumor, as well as lymph node involvement.

Right after the discovery of radium (^{226}Ra), radiation was already used to treat cervical cancer. Even today, radiation is the preferred choice for treating locally advanced cervical cancer. Treatment typically starts with a combination of chemotherapy and external beam radiotherapy (EBRT) to eliminate or shrink the tumor [4]. The EBRT treatment consists of 25 fractions of 1.8 Gy, 45 Gy for a complete EBRT treatment. As a second step, brachytherapy is applied. During the second half of the last century, several radium-systems were applied for brachytherapy. The radioactive stepping sources used today are ^{192}Ir or ^{60}Co [4]. The afterloader is responsible for managing, storing, and delivering the radioactive source to the target. Several computerized afterloader systems are used for brachytherapy of locally advanced cervical cancer [4]. In Department of Radiation Oncology at the Vienna General Hospital (AKH)/ Medical University Vienna (MUW) the brachytherapy treatment is usually divided into 2 times 2 fractions of HDR BT. In the first fraction, an applicator is inserted at the cervix and thus into the target area for two days. During treatment, the radioactive source is delivered through the applicator using the afterloader. In addition, interstitial needles can be used to help deliver the dose more precisely to the target area.

The gold standard is image-guided adaptive brachytherapy (IGABT) based on magnetic resonance (MR) imaging. Nevertheless, three dimensional (3D) computed tomography (CT) is also utilized, as many hospitals do not have the MR capacity or availability. The MR has better soft tissue imaging, were as a CT represents solid structures like bones, the applicator, and needles in a better way. Therefore, a new volumetric target concept based on MRI was introduced two decades ago. The resulting IGABT was evaluated in the EMBRACE studies and achieved excellent results [5], [6], [7]. These studies were conducted by a working group (GEC ESTRO - The Groupe Européen de Curiethérapie (GEC) and the European Society for Radiotherapy & Oncology (ESTRO)) with the goal of evaluating and comparing image-guided brachytherapy in prospective multicenter studies to establish a benchmark and improve

clinical outcomes. An overall 5-year local tumor control of 89% was shown for IGABT in RetroEMBRACE [7]. For EMBRACE I it was already 92% [6]. Furthermore, IGABT limited the overall major morbidity (G3-5) (3-6 % per organ in RetroEMBRACE and EMBRACE I) [5], [7], [8], [9].

As part of treatment planning, the target area, applicator, and surrounding OAR are defined by a radiation oncologist in the treatment planning system (TPS) in the MRI data set. The OARs are usually the bladder, rectum, sigmoid and bowel [4]. By defining dwell positions and dwell times in the applicator and needles, a 3D dose distribution can then be generated and optimized. In the following (second) fraction only a control MR is acquired, and an OAR assessment is made by a medical physicist and radiation oncologist. This is to show whether clinically relevant interfraction changes of the implant in relation to the tumor or the position and filling status of OAR have taken place. Studies with a large number of participants showed, that large systematic interfraction variations that cause a relevant increase of the dose to OAR usually do not occur [10]. However, sometimes there are exceptions. In these cases, interfraction motions require intervention of the planning team and an adjustment of the dose level.

Currently there are no purpose built-in solutions for rapid quantitative assessment of interfraction movements in a commercial TPS. One method for a quantitative estimation of the dosimetric interfraction variation of the OAR in a TPS is the very time-consuming landmark-based rigid image registration. In this case, the coordinate systems of the two MR images are synchronized using three equally selected applicator-based landmarks. With this method, the dosimetric interfraction variation can be recorded very accurately. In daily clinical practice it is difficult to use in terms of resources, especially in clinics with a high patient workload. This is due to the long time of >1h for manual evaluation of variations for each fraction.

In order to enable a rapid quantitative online evaluation of the dosimetric interfraction variation, Ecker et al. [11] have developed a research version of an automatic AI-based registration. Interfraction motion presents a significant challenge in BT and radiation therapy in general. The use of AI for rapid dose quantification enables timely interventions in case of dose discrepancies. However, the dosimetric accuracy of AI-based methods compared to manual methods in the TPS has not been evaluated so far. A thorough qualitative assessment of the clinical efficacy and safety is essential for its broader adoption.

Therefore, this thesis has the following two objectives. First is to assess inter- and intrafraction motion for a defined test cohort based on DVH parameters. Second is to evaluate the dosimetric impact of uncertainties in automatic registration methods.

2. THEORETICAL BACKGROUND

2.1 Cervical Cancer

2.1.1 DISEASE, STAGING & PREVENTION

Cervical cancer is mainly caused by persistent infection with HPV. There are currently 200 known types of HPV, and 12 of these types are classified as carcinogenic by the International Agency for Research on Cancer. HPV-16 is responsible for 50 % of cases; HPV-18 for 10 % of the cases [12]. Most infections are transmitted during adolescence or young adulthood [13]. However, infection is asymptomatic. So the first cervical changes often do not appear until 10 to 15 years after transmission [14] in many cases. About 80 % of women will be infected with HPV during their lifetime, with many infections occurring around age 45 [15].

There are behavioral and infectious factors involved in developing cervical cancer. Infections with HPV types that are responsible for cervical cancer can occur through sexual intercourse or through the mucous membranes. Therefore, lifestyle and sexual activity are important behavioral factors. The typical factors of risk for infection and development of cervical cancer are age at first sexual intercourse, a higher number of changing sexual partners, parity, smoking, co-infections, prolonged use of oral contraceptives and cervical dysplasia [16].

Staging of cervical cancer is the most important prognostic measure. Nodal status, tumor volume, depth of cervical stromal invasion and invasion of the lymphatic vascular space are necessary measures for staging. The most common staging systems are created by the International Federation of Gynecology and Obstetrics (FIGO) and the American Joint Committee on Cancer TNM system (tumor extent (T), lymph node involvement (N), and metastasis (M)) [17] (see Appendix Tab. 5).

Two different screening programs have been recommended for preventive care. Since 2008, the European Union (EU) has declared the Papanicolaou test (PAP test) and microscopic evaluation as the standard method [18]. This test is recommended by the EU to be done by every female person from the age of 20 in a cycle of 3-5 years [18]. In addition, this method is often combined with the HPV test, which is becoming more and more common.

In 2006, a breakthrough in the fight against HPV infection was achieved with the approval of the first HPV vaccine (four valent) by the US Food and Drug Administration [16]. Since then, cervical cancer rates have declined by 1% to 1.9% annually [12]. Although the vaccine cannot prevent an onset of disease in an existing infection, it does prevent further infection with other types. Due to the current problem that the first HPV vaccinations were approved in 2006, the vaccination coverage rate in Austria is still very low. The highest vaccination coverage rate was 53% among 14-year-olds in 2022. However, only 5% of the 21–30-year-olds are fully vaccinated

[19]. The importance of achieving higher levels of vaccination coverage to see the effects of herd immunity in this way. Therefore, even in highly developed countries, the treatment of cervical cancer remains a very important research topic.

2.1.2 OVERALL TREATMENT STRATEGY

The choice of treatment form is individualized for each cervical cancer patient based on several personal factors and a combination of methods. These include the stage of the cancer, whether and where the cancer has metastasized to other parts of the body, the size of the tumor and the patient's age and overall health [16]. For almost all tumor stages and grades, a multiple treatment regimen is chosen from a pool of different treatments (chemotherapy, EBRT, brachytherapy, and surgery). Tumors at FIGO stage IB1 and above are usually treated with a combination of chemotherapy, EBRT, and brachytherapy. In some cases, surgery is an additional option [20].

The standard chemotherapy regimen is cisplatin at a dose of 40 mg/m2 per week. Prerequisites are the patient's age, comorbidity, and morbidity. In 80% of the cases, this regimen is administered in 5 units [5].

Normally EBRT is also usually administered within 5 weeks. The goal is to deliver a 45 Gy dose to the tumor within 25 fractions. Both IMRT (Intensity Modulated Radiotherapy) and VMAT

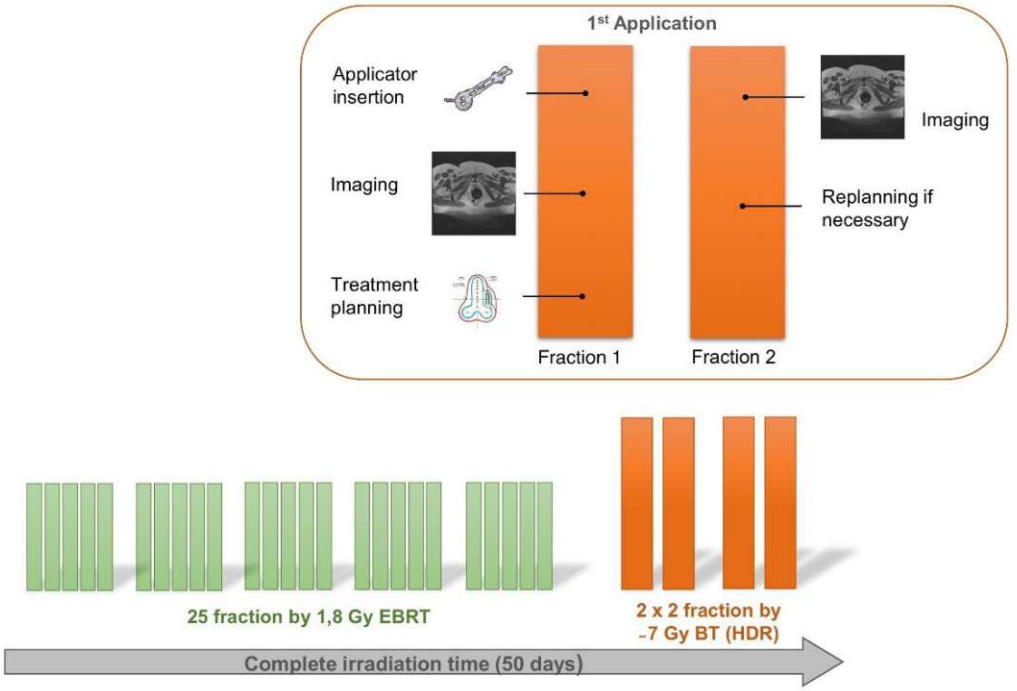

Fig. 1 Workflow for cervical cancer irradiation: Consists of 25 fractions of 1.8 Gy EBRT and 2x2 fractions of 7 Gy HDR BT. During an application, the applicator is inserted in the first fraction and remains in place for the entire application. This is followed by imaging and treatment planning. Prior to the second fraction, imaging is performed again, and replanning is performed if necessary. [courtesy of S.Ecker]

(Volumetric Modulated Arc Therapy) techniques are used. For a closer look at EBRT techniques in cervical cancer treatment, we recommend the EMBRACE II study [5]. EBRT is followed by HDR-BT (details in chapter 2.2.1), which consists of two times two fractions of approximately 7 Gy per fraction. For this treatment, an applicator is inserted into the cervix for each of the two fractions. CT or T2-weighted MRI can be used for 3D imaging to determine the targets and OAR, as well as the position of the applicator in the TPS. In some cases, only 2D-based radiographic planning is used. Currently, most clinics worldwide use CT-based 3D planning [21]. The main reason for this is the better availability and capacity of clinics for these devices. Due to the significantly better soft tissue contrast, which is important for the target definition and mapping of the OAR, planning with MRI is the recommended gold standard [22] and has proven to be the method of choice in the EMBRACE studies [5], [6], [7].

On day 2 another MRI scan is performed before starting the second radiation treatment. This is necessary to check for relevant shifts of the OAR or the applicator between first and second fraction. This control is often done visually. In case of uncertainty or dosimetrically relevant OAR shifts, a new plan has to be developed (details in chapter 2.4.1) [4]. These differences are called interfraction variations. After a one-week break, the whole process is repeated for the third and fourth fractions [4].

The standard irradiation workflow for cervical cancer, as it has evolved at the Department of Radiation Oncology of the AKH /MUW due to historical developments and economic factors, is shown in Fig. 1.

2.2 State of the art Brachytherapy

2.2.1 HARDWARE

Brachytherapy for cervical cancer requires two main hardware components. One is the afterloader, which contains and controls the radiation source. It is the device to which the channels of the applicator and the needles can be connected, and which ensures precise dosing and placement of the radiation previously defined in the TPS. The radioactive source is welded to a cable that can be moved through a guide tube into the body region under computer control. It is stopped at dwell positions for the dwell time and thus the target region is irradiated. Four different dose-rate techniques are available for the afterloader. All of them use sources with different radiation levels, which affects planning and dwell times. The variants can be classified as follows:

- low-dose rate (LDR): below 1 Gy h^{-1}
- intermediate-dose rate (MDR): between 1 Gy h^{-1} and 12 Gy h^{-1}
- high-dose rate (HDR): above 12 Gy h^{-1}
- pulse-dose rate (PDR): multiple HDR pulses of 0.5 Gy to 1 Gy separated by time intervals of approximately 1 h [23]

Fig. 2 left: a tandem and ring applicator with interstitial catheters and right: a tandem and ovoid with interstitial catheters [25]

For HDR and PDR, ^{192}Ir with its high specific activity is used. It has a half-life of 74 days and is replaced every three months in clinical use. Otherwise the radiation times would become too long [4]. The radioactive material is encased in a stainless steel capsule. This stops low-energy electrons released during decay and prevents contamination. PDR is gentler on the organs because of the lower pulse dose. LDR treatment is not used for cervical cancer brachytherapy [24].

In the case of cervical cancer treatment, one of two applicator types is usually used: a tandem and ring applicator or a tandem and ovoid applicator (Fig. 2). The applicator is inserted intracavitarily, i.e. without tissue damage, during a surgical procedure. Modern models offer guidance options for interstitial needles. Needles are inserted into target regions when required by the tumor structure. Tandem and ring applicators from Elekta (Veenendaal, The Netherlands) were used as standard at the Department of Radiation Oncology of the AKH /MUW [25]. The Tandem primarily covers the body of the uterus, allowing the ring to irradiate areas around the cervix [26, p.589].

2.2.2 MR IMAGE-GUIDED ADAPTIVE BRACHYTHERAPY

The insertion procedure is followed by a three-dimensional T2-weighted MRI scan with the applicator in place. In order to determine where the dwell positions of the radioactive source are feasible for treatment planning, the exact position of the applicator must be reconstructed in the image set [27]. In modern TPS, 3D models of the applicators with the exact source paths are available. The reconstruction of the applicator can be divided into two steps [4], [28]. First, the applicator model used with the corresponding afterloader is selected from the TPS library. In the second step, the virtual applicator model is moved and rotated into the corresponding structure within the image set. Attention is paid to the fusion of the applicator model shape model until it is in alignment with the applicator visible in the image set, such as parts of the source path or the outer surface of the applicator [4]. The model is placed into the image set layer by layer. Reconstruction of the applicator is more difficult in MRI than in CT because the applicator, which is made of hardened plastic, does not yield any signal on MRI. The MRI slice

thickness should be ≤ 5 mm to ensure the accuracy of the reconstruction [27]. An example is shown in Fig. 15.

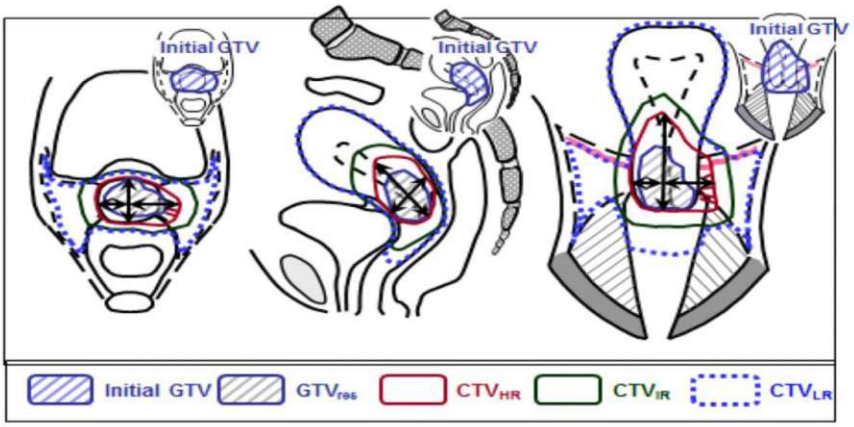

Fig. 3 target concept: schematic diagram for EBRT and brachytherapy targets in cervical cancer, stage IIB bulky disease and good response after chemo-radiotherapy: coronal, transversal and sagittal view. Brachytherapy targets: limited GTV-T_{res} (residual GTV after EBRT), adaptive CTV-T_{HR}, and CTV-T_{IR} (GTV-T_{init} plus margins around the CTV-T_{HR}). Maximum width, thickness, and height of the adaptive CTV-T_{HR} are indicated [5].

Subsequently, the treating oncologist contours the target according to an adaptive target concept (see Fig. 3). It defines the target area after EBRT has been performed. The resulting clinical high-risk target volume (CTV-T_{HR}) is defined based on the remaining gross tumor volume (GTV) and grey zones on T2-weighted MRI. These grey zones indicate regions of high risk for microscopic disease, especially in the tumor area prior to EBRT. This CTV-T_{HR} is considered the main target volume in IGABT. In the more advanced stages of the disease, the vagina and other organs may be part of the CTV and therefore included in the target area [4]. The ICRU Report No.89 [4] and the EMBRACE II [5] study provide a detailed description of the target areas.

The dwell position and dwell time of the radiation source are determined by a medical physicist according to the planning objectives and maximum OAR values (details in chapter 2.3.3). Also the dose exposure that has already happened during EBRT is considered. The created treatment plan is permanently optimized by evaluating both the isodoses and dose metrics and adapting the dwell times accordingly.

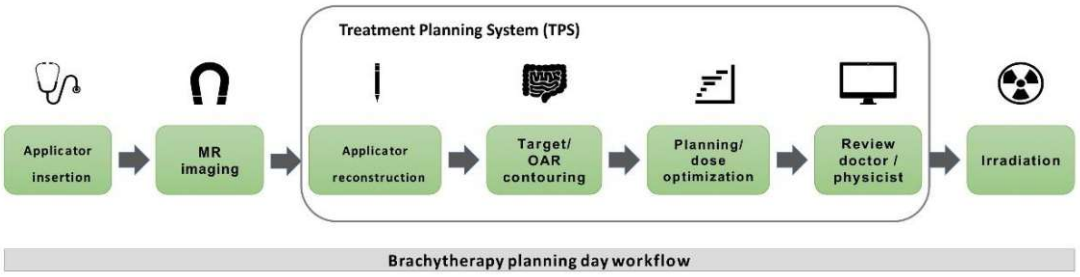

Fig. 4 Planning day workflow: At the beginning of the day, the applicator is inserted through a surgical procedure. This is followed by a pelvic MRI. With this MRI, the applicator is first reconstructed in the TPS, then the target and OAR are contoured, and the dose is calculated and optimized. This is reviewed by a medical physicist and a radiation oncologist, and then the radiation is delivered.

Prior to irradiation, the plan was cross-checked by the medical physicist and the oncologist [4] .

Once all hardware components are connected and the planning is completed, the radioactive source is passed through connected channels (up to 20) of the afterloader. It is stopped at the specified dwell positions for the respective dwell time [23].

2.3 Dose prescription and dose optimization

The main goal is to irradiate each tumor cell as effectively as possible with the required dose. However, it is important to note that organ cells should be exposed to the lowest possible dose during irradiation. There are several challenges to dose response calculation and treatment planning. One of the main difficulties is the dose summation between EBRT and BT, which is crucial for estimating the overall treatment effect. The two techniques differ mainly in two aspects - spatial dose distribution and temporal dose characteristics. Computational models are used to solve this problem. The way the tissue absorbs the radiation and the difference between the absorbed dose and the dose influenced by the biological effect (biological dose) must be considered. This is considered to determine the clinically relevant dose exposure of an OAR. The most accurate way is to calculate the biological equieffective dose for each cell in each fraction of EBRT and BT and add them up. From a technical perspective this means to calculate the equieffective dose for each voxel in each fraction of both techniques and to sum the doses using a formalism. However, in practice it is not possible to high-precisely pair voxels in EBRT and BT images due to the anatomical changes brought about by the presence of the applicator and the shrinking of the tumor. A promising technical implementation to solve this problem is deformable image registration (DIR) (see chapter 2.5), which in principle can account for anatomical changes. However, DIR changes the voxel-to-voxel relationship, and the resulting uncertainties are difficult to estimate. Currently available algorithms do not address the complexity of the task, and the use of DIR for dose summation in clinical practice is not recommended [29].

In cervical cancer treatment planning practice, a simplification method for dose accumulation is used. The simplification that can be made by summing EBRT and BT is that it can be assumed that the clinically relevant areas of the organs (and targets) will all receive the same/homogeneous EBRT dose. The justification for this is that these areas are all very close together, in the immediate vicinity of the applicator. This worst case assumption allows the DVH parameters to be simply summed [4].

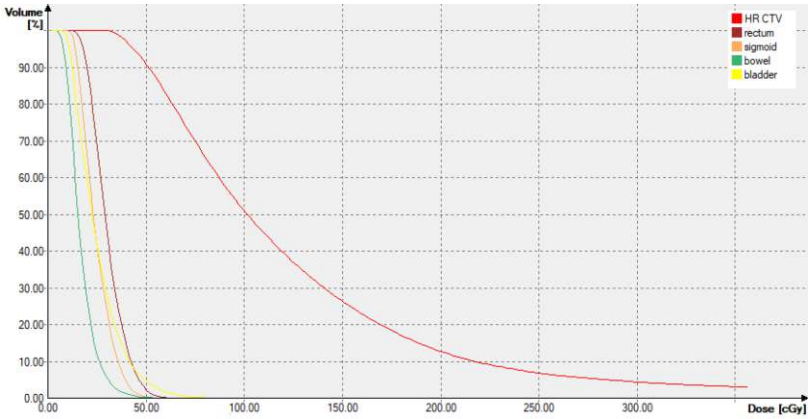

Fig. 5 Dose-volume histogram of a brachytherapy treatment. The DVH plots the absorbed dose on the horizontal axis and the percentage of tissue or organ volume that receives or exceeds that dose on the vertical axis. Each point on the DVH therefore represents a percentage of the volume that receives a certain dose. [courtesy of D.Neugebauer]

Dose-volume histograms (DVH) have been recommended as an illustration and calculation basis for the dose distribution of cervical cancer. The dose value achieved at least in a certain volume fraction can be read from a DVH. A DVH is a cumulative histogram where summing begins at the maximum dose received by the structure. A DVH can therefore be used to determine the minimum dose value achieved in each volume fraction. The ideal DVH for radiotherapy shows a steep drop in dose as a percentage of volume, meaning that most of the tissue receives a low dose and only a small amount receives a higher dose. In radiotherapy, DVHs are used to ensure that the radiation dose is precisely targeted to the target tissue to achieve the maximum effect on the tumor while sparing the surrounding healthy tissue as much as possible. The DVH is also a dose statistics tool and can be used to assess treatment plan quality and to optimize dose distributions. A general problem for considering the DVH parameters is that it is not possible to know at which point the dose is located within this volume. Based on the linear DVH addition, the dose planning aims can be defined for the entire radiation treatment (2.3.3). They are classified as soft planning targets and hard dose constraints [5].

2.3.1 EQUIEFFECTIVE DOSE IN 2 GY FRACTIONS (EQD2)

The irradiation effect on tissue depends on various clinical and biological factors. These include dose rate, dose per fraction, break time between fractions and pulses, overall time, radiation quality, and patient- and tumor-related factors.

Information's in this chapter are based on the book Basic Clinical Radiobiology by Joiner and Kogel et al. [30] and the ICRU Report 89 by Pötter et al. [4]. In the following, a short overview of the effect of irradiation on the cell will be given.

Ionizing radiation has two different effects on a cell. A cell can either be directly affected by the radiation or through the formation of free radicals. In this case, the DNA structure of the cell gets damaged and oxidative base damage occurs, which can be followed by single strand breaks or even double-strand breaks. In this situation a cell has different possibilities to repair

base damage and single-strand breaks. Double-strand breaks, however, can cause mutations and can lead to cell death. This process is used to target tumor cells.

LINEAR QUADRATIC MODEL

To understand the relationship between absorbed dose (D) and survival (S) in front of different tissue types, several tissue column formation studies were performed [28, p.106]. Cell clusters of the same tissue type were irradiated with different absorbed doses and the mathematical factors α ([α] = Gy^{-1}) and β ([β] = Gy^{-2}) were introduced. These serve as constants for the tissue types in the calculation of survival rates. In this case the factor α maps the linear components of cell survival, while β maps the quadratic components. The calculation of the survival rate is described in the linear-quadratic model and can be expressed in the following formula:

$$-ln\,(S) = \alpha D + \beta D^2 \tag{1}$$

A basic division into two categories is made when considering tissues. On the one hand, there is the so called late-responding tissue. This tissue type is known for a low α/β -ratio (0.5-6 Gy), which comes with a high repair capacity. However, damage to these tissues can still occur months after the irradiation [28, p.106]. These tissue types include the healthy organ walls of the OAR in brachytherapy as well. On the other hand, there are acute-responding tissues, which have a low repair capacity and therefore suffer damage during irradiation very quickly. They have a high a α/β -ratio of 7-20 Gy [28, p.106]. Both tumor tissue in the cervix and mucous membranes belong to this type.

EQUIEFFECTIVE DOSE

The equieffective dose helps to generate a comparable dose effect by considering the fraction-related biological effect of the different irradiation techniques. The calculation is also based on the linear-quadratic model discussed above [31]. and implies the tissue factor of the α/β -ratio, the total absorbed dose D and the absorbed dose per fraction d.

$$EQDX_{\alpha/\beta} = D * \frac{d + \alpha/\beta}{X + \alpha/\beta} \tag{2}$$

Consideration of EQDX for an X of 2 Gy has historically evolved as the standard reference dose. Reason: Most patients treated with external photon beams receive fractions of 2 Gy, 5 times

a week. A very large body of experiences and relationships are well established between this dose and the likelihood of a particular clinical outcome. Thus, EQDX is widely accepted as a reference in radiation oncology. Equieffective absorbed dose EQD2 assumes that when two or more irradiation plans are compared, the reference treatment is 2 Gy per fraction.

The GEC-ESTRO has recommended the α/β ratio for cervical cancer to amount to α/β = 10 Gy for target tissue and α/β = 3 Gy for the tissue of the OAR [4], [32].

2.3.2 DOSE VOLUME PARAMETER

Classically, the DVH parameter for the target area was described as the absolute minimum volume deviation at D_{100}. The D_{100} value represents the minimum dose received by the structure. The D_{90} parameters proved to be much more stable against uncertainties. In this respect, it makes more sense to examine the D_{90} value, even though 10% of the target volume will receive a lower dose [4]. The minimum target absorbed dose depends very much on the volume reconstruction and the absorbed dose sampling in the TPS, therefore the D_{90} is used instead of the D_{100} [4], [33]. Another parameter that has proven to be useful and robust is the near-minimum dose D_{98}. Schmid et al. [33] showed that there can be significant differences between D_{98} and D_{100} due to the gradients of absorbed dose in brachytherapy. Thus, a direct comparison between these two closely related values is impossible [33]. High dose volumes for intracavitary brachytherapy contribute to the excellent local control observed even in large-volume disease [4], [34]. Heterogeneity of brachytherapy dose is substantial in the target region with typically absorbed dose gradients ranging from 5% to 25% mm^{-1} [4] .

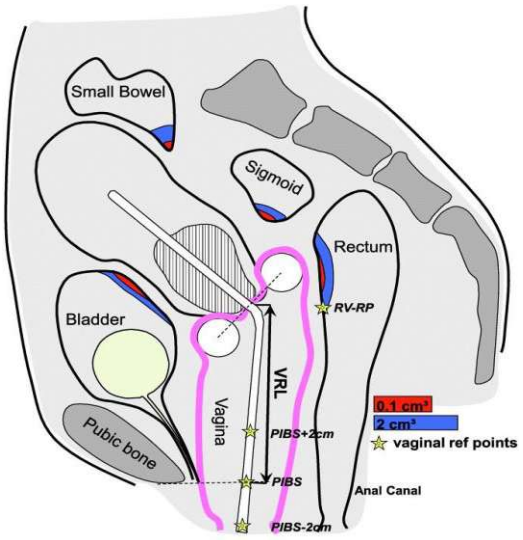

Fig. 6 Position of OAR with the illustration of D0,1 and D2 (sagittal view) [34]

DVH parameters are used in OAR for planning and evaluation as well. However, in this case the aim is to minimize the irradiated volume and, most importantly, not to stress the organ walls. There is a common risk for side effects of HDR-BT (see chapter 2.3.3) such as local

inflammation, fibrosis, telangiectasia, ulceration, necrosis, and fistulae increases at the wall [32]. Since the affected organs are hollow organs, the filling state of the respective organs should be considered. For valid and reliable data collection, the degree of filling should be as consistent as possible. This appears to be especially important for the bladder, as this can change within short periods of time [34], [32]. Because the dose rapidly decreases near the radiation sources (especially in adjacent small organ (wall) volumes), dose assessment has to be carried out based on defined dose points for these confined volumes. The recommended volume observation points for the maximum dose values for the OAR are determined for the volumes 0.1 and 2 cm^3 of the most irradiated tissue volumes adjacent to the applicator [32]. Thus, the $D_{0.1cm^3}$ and D_{2cm^3} are used as reference parameters for the OAR, i.e., the minimum dose in the $0.1cm^3$ and $2cm^3$. These volumes receive the highest dose of the organ.

2.3.3 DOSE PLANNING AIMS

In local tumor control, dose-response curves are useful for understanding the relationship between the dose of radiotherapy administered and the response of the tumor. They help determine the optimal dose for treatment, predict efficacy, optimize treatment sequences, or develop new therapies, and assess side effects. As noted above, achieving the desired tumor control dose goals without exceeding the morbidity endpoints of the OAR is the goal of treatment planning guidelines [5] and can be depicted in dose-response curves. At the same time, a dose-response curve for the probability of tumor cell survival must be considered. The current dose-response curves of Schmidt et al. [35] for D90 of CTV_{HR} are shown in Fig. 7.

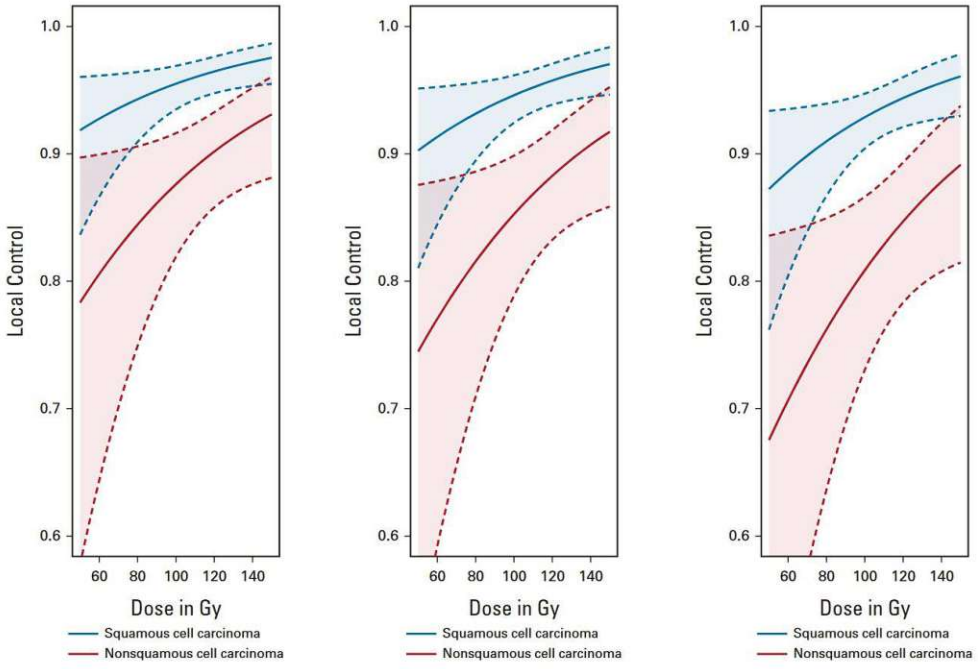

Fig. 7 Dose-response curves for D_{90} of CTV_{HR} for the end point of local tumor control plotted based on CTV_{HR} groups: (left) CTV_{HR}, 20 cm^3, (middle) CTV_{HR} 20-40 cm^3, and (right) CTV_{HR}. 40 cm^3; blue line: squamous cell carcinoma, red line: adeno- or adenosquamo and dotted lines: 95% CIs. CTV_{HR}, high-risk clinical target volume; D_{90}, minimal dose to 90% of the respective target volume. [35]

The dose-response curves are affected by uncertainties in dose reporting. These can be caused by various circumstances, such as the use of different TPS and evaluation software for DVH [36] or interfraction variation as the main source of uncertainty [10], [37], [38] (see chapter Adaptive Treatment Planning). Therefore, there is a need to reduce uncertainties for a better dose-response assessment.

These curves are based on the established treatment with specific planning targets for the individual DVH parameters of targets and OAR. As described in Chapter 2.3.1, the planning goals include the total dose from EBRT and brachytherapy in EQD2. In this context, linear DVH addition is the current standard procedure for the summation of both procedures [39].

In an extensive multicenter database analysis of patient data from several hospitals, EMBRACE II established planning objectives. The recommended values from this become the reference value and for targets can be seen in Table 1 [5]. For target areas, $D_{98\%}$ is used the most stable value against uncertainties such as contouring inaccuracies. In addition, the $D_{90\%}$ in CTV-T_{HR} represents the dose in the central part of the tumor and thus the area with the highest tumor cell density [40]. The relevance of the values of each target increases from right to left in Table 1 [40].

Target	D90 CTV_{HR}	D98 CTV_{HR}	D98 GTV_{res}	D98 CTV_{IR}	Point A
Planning Aims	>90 Gy	>75 Gy	>95 Gy	>60 Gy	>65 Gy
Limits for Prescribed Dose	>85 Gy	-	>90 Gy	-	-

Table 1 Hard and soft contains for the treatment planning in EMBRACE II. All dose parameter show the EQD2, which is calculated using $\alpha/\beta = 10$ for targets. The total EQD2 include 45 Gy/25 fractions delivered by EBRT. [5]

For the OAR, the dose planning aims are represented by $D_{0.1cm^3}$ and D_{2cm^3}. They are shown in Table 2.

OAR	Bladder D_{2cm^3}	Rectum D_{2cm^3}	Recto-vaginal point	Sigmoid D_{2cm^3}	Bowel D_{2cm^3}
Planning Aims	<80 Gy	<65 Gy	<65 Gy	<70 Gy*	<70 Gy*
Limits for Prescribed Dose	<90 Gy	<75 Gy	<75 Gy	<75 Gy*	<75 Gy*

Table 2 Hard and soft contains for the treatment planning in EMBRACE II. All dose parameter show the EQD2, which is calculated using $\alpha/\beta = 3$ for OAR. The total EQD2 include 45 Gy/25 fractions delivered by EBRT. [5]

* For the sigmoid/bowel structures these dose constraints are valid in case of non-mobile bowel loops resulting in the situation that the most exposed volume is located at a similar part of the organ. [5]

2.4 Adaptive Treatment Planning

2.4.1 INTRA- AND INTERFRACTION VARIATIONS

In cervical cancer treatment (both EBRT and BT), there are many different uncertainties that can cause an error between the planned dose and the dose delivered to each target and OAR. For BT, errors include source calibration, dose and DVH calculation, applicator reconstruction, contouring, dose delivery, and intra- and inter-fraction uncertainties [41]. Both the uncertainties in general [41], [42], [43], [37], [44] and the inter- / intrafraction variations [10], [38] for MR-guided adaptive techniques are of interest to different research groups. The reason is they can have a large dosimetric influence (see 2.4.2). Fraction-dependent variations are distinguished between interfraction variations and intrafraction variations. The interfraction variations describe the variations that occur between creating the planning MR and the control MR on the following day (approx. 24 h). Because it is common practice in brachytherapy to represent the minimum dose received by the structure., interfraction variations may occur [41]. The intrafraction variations on the other hand are those variations that occur in one fraction during the treatment over a very short period of approx. 45 min. These variations are caused by the mobility of both the OAR and the targets with the in the abdomen. This variation can be seen schematically in Fig. 8.

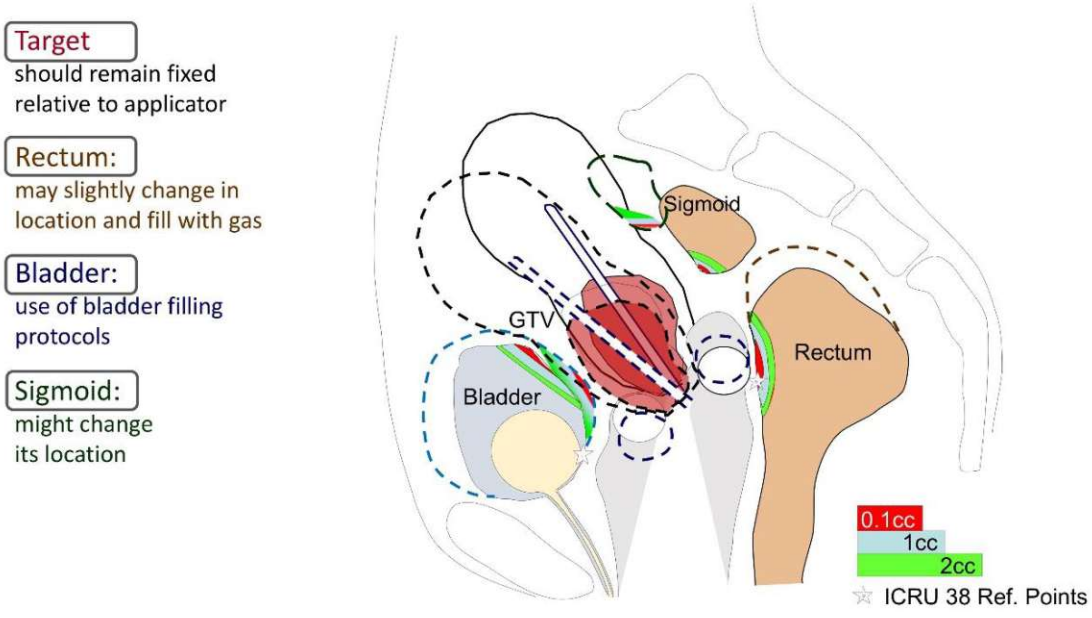

Fig. 8 Expected inter- and intrafraction variations for cervix brachytherapy (sagittal view) [courtesy of Nicole Eder-Nesvacil]

In addition, in rare cases, the applicator itself may move within the cervix. This can also cause dose variation, even if the applicator is firmly attached to the target area, so no significant dose variations are expected. It turned out that the posterior inferior bladder wall and the

anterior rectal wall are relatively fixed in relation to the applicator. Sigmoid loops, however, have more room to move autonomously from the cervix/uterus and the applicator [10].

In addition, the volume of adjacent organs may change during fractionation or between fractions. Since all OAR are hollow organs filled with substances of different aggregate states, their volume might change very rapidly. This can be attempted to be regulated via catheters. The bladder catheter is usually placed during treatment. Thereby, the bladder filling volume is adjusted according to bladder filling protocol. At the Department of Radiation Oncology of the AKH /MUW this volume is 50 ml. However, it is possible that the bladder has already refilled again in the time between the insertion of the catheter and the MRI or radiation. These volume differences can be considerable (see Fig. 9)

For the different areas of the colon, the volume changes mainly occur due to air bubbles. In this case, the air can be released through a rectal catheter.

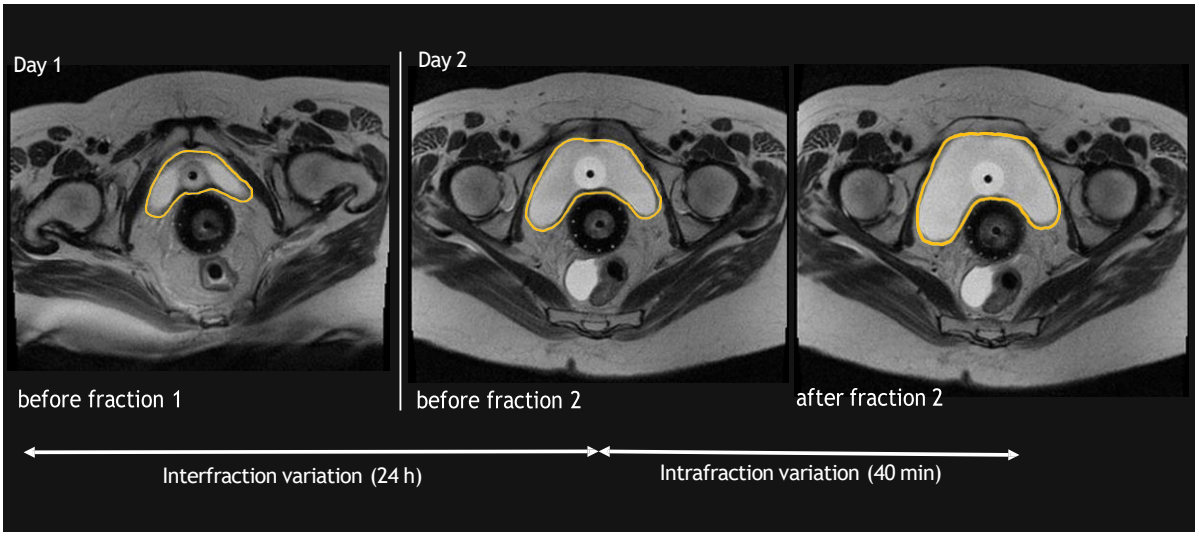

Fig. 9 Bladder volume growth at different fraction time points

Due to the very high dose gradient in brachytherapy, the volume change or shift can have a very large influence on the $D_{0.1cm^3}$ and D_{2cm^3} of the organ walls. It may not be relevant if the change is on the side of the OAR away from the applicator. This must be evaluated.

2.4.2 DOSIMETRIC EVALUATION OF INTRA- AND INTERFRACTION VARIATIONS

According to Kirisits et al. [42], the typical level of inter- / intrafraction variations for intracavitary IGABT treatment of locally advanced cervical cancer (LACC) is 11% of the CTV-HR D_{90}. These findings account for a large proportion of dosimetric uncertainties. The inter/intra-fraction variation may be statistical or systematic and may have different causes, e.g.,

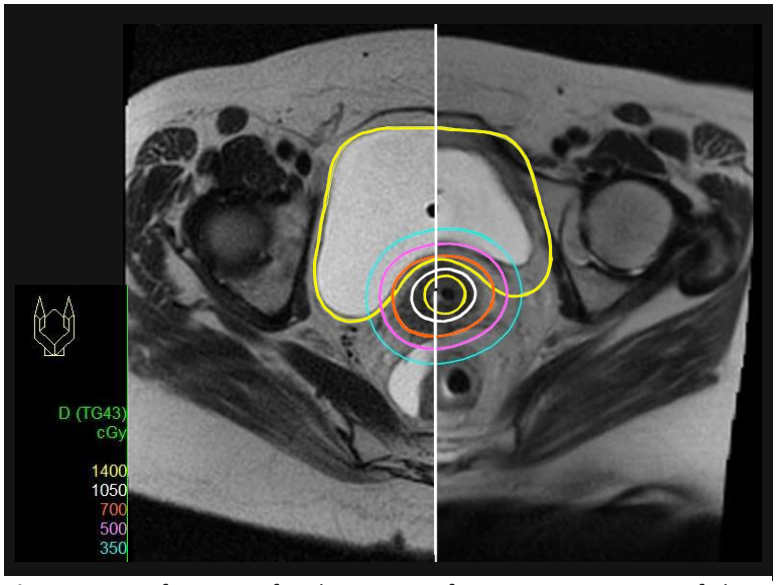

Fig. 10 Significance of volume interfraction variations of dose exposure on the bladder - created in Oncentra® Brachy

uncertainties in technical afterloader parameters, applicators, or organ motion. This can have different effects on the targets and the OAR [42]. A good reference overview of the variations in Gy_{EQD2} was provided by the study of Nomden et al. [38] shown in Table 3.

Another anatomically assumed finding in terms of the variations is the random uncertainties/ mean ± standard deviation (SD) of the relative D_{2cm^3} observed by Nesvacil et al. [10]. They were defined for the sigmoid/bowel with 1.6 Gy ±26.8%. This is clearly larger than the rectums SD (4.1 Gy ±21.7%) or the bladders SD (0.6 Gy ±19.5%). Overall, the total variances provided in this study are slightly higher than the ones Nomden et al. [38] stated. However, both studies provide an important reference for the dosimetric assessment of inter-/intrafraction variations. As expected, the amount of intrafraction dose deviations in the Mean are somewhat smaller than the interfraction dose deviations. However, as the SD of the two studies by Nomden et al. [38] and Nesvasil et al. [10] show, there are always cases in which the intra- and interfraction variations have a strong dosimetric influence. These must be recognized.

Table 3 Dosimetric variations for D90 HR-CTV, D_{2cm^3} bladder, rectum and sigmoid. Mean differences, standard deviations, minimum and maximum values for different time intervals and calculated for the differences between total estimated and total planned dose [42]

HDR

Planning interval						Irradiation interval					
n=30	Gy_{EQD2}	Mean	SD	Min	Max	n=26	Gy_{EQD2}	Mean	SD	Min	Max
HDR-CTV		-0.1	0.5	-1.2	1.4	HDR-CTV		0.2	0.7	-1.0	2.1
Bladder		0.1	1.1	-2.6	3.3	Bladder		-0.1	1.0	-2.2	3.1
Rectum		0.4	1.5	-2.3	6.0	Rectum		-0.1	0.7	-2.2	1.8
Sigmoid		0.4	1.2	-2.7	2.9	Sigmoid		-0.1	1.2	-2.6	3.7

Day interval						Total estimated dose - total planned dose					
n=30	Gy_{EQD2}	Mean	SD	Min	Max	n=15	Gy_{EQD2}	Mean	SD	Min	Max
HDR-CTV		-0.1	0.7	-1.8	1.4	HDR-CTV		-0.4	2.1	-4.3	2.9
Bladder		-0.3	1.6	-5.0	4.4	Bladder		-0.3	3.8	-8.5	5.4
Rectum		0.7	1.4	-2.9	4.0	Rectum		2.1	4.0	-5.3	10.2
Sigmoid		0.1	1.3	-2.1	3.9	Sigmoid		0.9	2.9	-5.7	5.5

Planning = D (MRpre-irrad) - D (MRplan)
Irradiation = D (MRpost-irrad) – D (MRpre-irrad), day = D $(MRpre\text{-}irrad)_{day2}$ - D $(MRplan_{day1})$.
Total planned dose = D (EBRT) + 2 x D (MRplan BT1) + 2 x D (MRplan BT3).
Total estimated dose = D (EBRT) + D (MRpre-irrad BT1) + D (MRpre-irrad BT2) + D (MRpre-irrad BT3) + D (MRpre-irrad BT4).

2.5 Registration methods

A medical image is a representation of the internal structure or function of an anatomical region in the form of an array of picture elements called pixels or voxels. It is a discrete representation is the result of a scanning/reconstruction process in which numerical values are mapped to positions in space. The level of detail with which anatomy or function can be represented is expressed by the number of pixels used to describe the field of view of a particular imaging modality [45], [46].

Medical image file formats can be divided into two categories. The first category includes formats designed to standardize images generated by diagnostic modalities, such as DICOM (Digital Imaging and Communications in Medicine). The second category includes formats designed to facilitate and improve post-processing, such as Analyze and NifTi (Neuroimaging Informatics Technology Initiative). DICOM and NifTi formats were used in this thesis.

Image registration involves searching for a spatial transformation to match the points of a moving image with those of a fixed image. The basic process is shown in Fig. 11 and illustrated below using elastix, a publicly available computer program for intensity-based medical image registration [46]. The information in this paragraph is taken from the elaboration by Akinrimisi [45] and the elastix structure by Klein et al. [46]. Often the image complexity is reduced by applying a pyramid that smoothes and, if necessary, downscales. This makes it easier to find an initial alignment, which can then be further optimized. The fixed image is sampled, whereby randomly selected coordinates can be used instead of all pixels to speed up the process. These

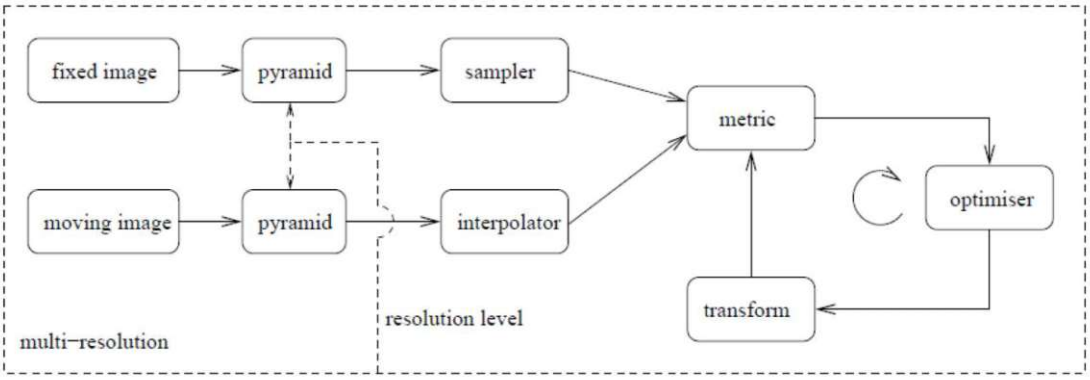

Fig. 11 Basic registration components. The scheme is an simplified version of the scheme introduced in [46]

coordinates can be either pixel positions or interpolated pixel positions. The moving image is evaluated at non-pixel positions, so an interpolator is applied, usually an Nth-order B-spline interpolator, whose complexity can be adjusted to achieve a balance between quality and speed [45], [46]. The metric or cost function evaluates the quality of the alignment between the fixed and moving image and is based on a similarity term as well as a penalty term. There are different metrics that can be used depending on the situation. If the images are from the same modality, the mean square difference (MSD) can be used. A general metric is the mutual information (MI), which assumes a relationship between the probability distribution of the fixed and moving image and allows multimodal registration [45], [46]. The moving image is then deformed by a transformation so that it matches the fixed image; examples of transformations are rigid, affine, and non-rigid.

Rigid: A rigid transformation allows a translation and rotation of the moving image but does not allow for any change in size or shape. This means that the image can only be moved and/or rotated without allowing deformation.

Affine: The affine transformation is more flexible than the rigid transformation. It allows translation, rotation, scaling and shearing of the image. In contrast to rigid transformation, however, the affine transformation preserves collinearity, i.e. all points that lie on a line remthein on a line even after transformation (parallel lines remain parallel). In addition, ratios of distances along parallel lines are preserved, which means that the center of a line segment remains the center even after the transformation.

Non-rigid: The non-rigid transformation does not preserve the shape of the image. The image can be stretched or compressed in any direction, which enables local deformations [45]. However, since this is a more complex transformation, it can be slower to achieve, and the transformation is optimized to minimize the cost function. The choice of an optimizer affects the speed and accuracy of image registration [45], [46].

To evaluate possible uncertainty factors, it must be considered which basis should be used for the image registration. Since the dose in brachytherapy is tied to the applicator, it has been found to be useful to use the applicator as the basis for registration. The most commonly used clinical method, which has been shown to be very accurate in BT, is manual registration using landmarks [47]. But research on the much faster automatic applicator-based registration algorithms is still in progress [48].

MANUAL RIGID APPLICATOR-BASED IMAGE REGISTRATION

Using the applicator as a fixed registration base has proved useful for BT. On the one hand, it is an unchanging component and, more importantly, the dose is linked to it. In order to perform manual rigid applicator-based image registration, it is essential for BT to reconstruct the applicator within the TPS image sets. To do so, reconstruct the applicator in both image sets being registered as described in chapter 2.2.2.

Conventional TPS now offers a point matching algorithm as an image registration option that can register the two image sets based on the set of corresponding landmarks. To perform the registration, at least three reproducible fixed points, so-called landmarks, are defined in the two image data sets to be registered. Landmarks that refer to the applicator are ideal for this purpose. Using the corresponding landmarks, the point matching algorithm now rigidly aligns the image sets. Both images can be superimposed to check the registration.

IMAGE REGISTRATION BASED ON AUTOMATED APPLICATOR RECONSTRUCTION

The information used in this section for the overview of machine learning is taken from Lundervold et al. [49] and Goodfellow et al. [50]. Machine learning encompasses a range of methods that enable computers to solve problems by learning from data, aiming to develop mathematical models capable of making accurate predictions on new, unseen data. Common types include supervised, unsupervised, and reinforcement learning. Artificial neural networks (ANNs) are one of the most popular machine learning models. Recently, research on automatic algorithms based on neural networks has been advanced in medical imaging [28], [49]. A neural network consists of layers of interconnected neurons that pass data through the network. There is an input layer, hidden layers for data processing, and an output layer for predictions. The network is trained by identifying patterns in training data and adjusting its parameters accordingly This is done by using an optimization algorithm called gradient descent on a function that measures the correctness of the outputs and minimizes it, called

the cost function or loss function. The basic form of artificial neural networks, feedforward neural networks, are parameterized mathematical functions $y = f(x; \theta)$ that map an input x to an output y by passing it through a series of nonlinear transformations: $f(x) = (fn \dots fn)(x)$. Each component fk, called the grid layer, consists of a simple linear transformation of the output of the previous component followed by a nonlinear function: $fk = \sigma k(\theta T\ k\ fk\text{-}1)$. The non-linear functions σk are usually sigmoid functions and the θk are numerical matrices called model weights [49]. During the training phase, the network is fed training data and asked to make predictions at the output layer that match the known labels. Training a neural network means changing its weights to optimize its output.

Neural networks are now the basis for most deep learning algorithms. In deep learning, computers automatically learn useful representations and features directly from the raw data, bypassing the difficult step of extracting them manually. The discovery of features and the performance of a task are combined into a single problem and therefore improved during the same training process. In medical imaging, interest in deep learning has been sparked primarily by convolutional neural networks (CNNs) [51], a powerful method for learning useful representations of images and other structured data [49].

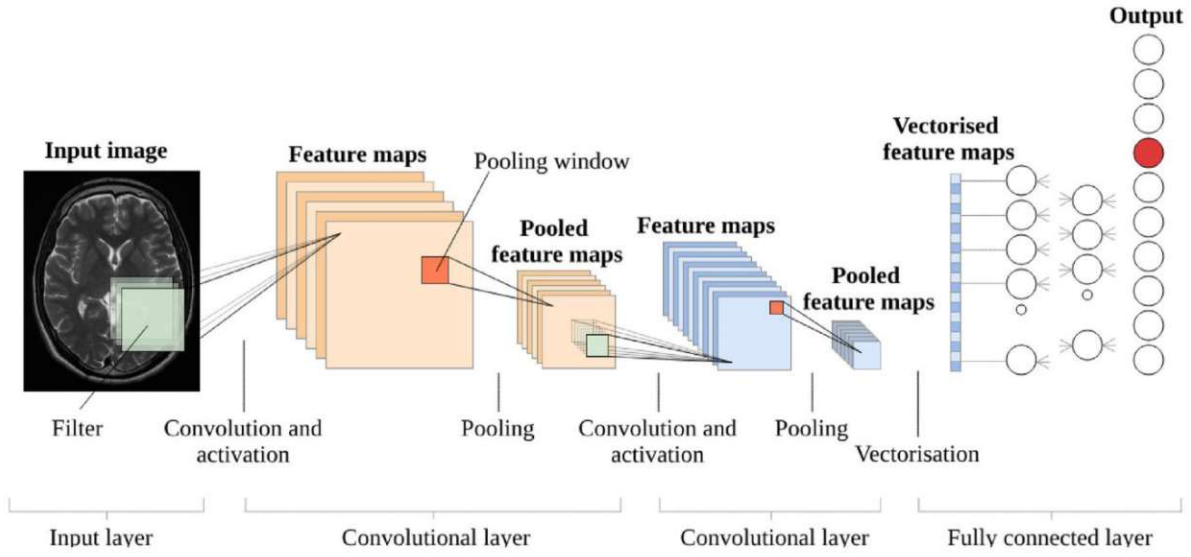

Fig. 12 Building blocks of a typical CNN [49]

The information about CNN also comes from the paper by Lundervorld et al. [49]. CNN is a specialized neural network designed specifically for image processing. Unlike conventional feedforward networks, CNNs have a structure that preserves the spatial relationships in the data, allowing them to better exploit the three-dimensional structure of images. A CNN consists of multiple layers of convolution and activation, often with pooling layers, and is trained using backpropagation and gradient descent. Convolutional layers apply convolutional operations to the input data to extract features. These convolutional layers use small filters to detect local patterns in the images. The results are then passed through activation functions to allow for nonlinear responses. Pooling layers are used to reduce the dimensionality of the

data and improve computational efficiency. This is typically done through methods such as max-pooling or average-pooling, where small regions of the data are pooled together. In addition, dropout regularization and batch normalization techniques can be applied to make the CNN more robust and reduce overfitting. Dropout randomly removes some neurons during training, allowing the network to adapt to different aspects of the data, and batch normalization ensures that layer activations are stabilized, resulting in faster training and improved generalization. Over time, several architectures have evolved that use CNN. For example, there are YOLO [52], ResNet [53], SENets [54], as well as V-net [55] and U-net [56]. The latter has proven to be very successful for training on medical images [57].

The AI-based applicator reconstruction algorithm trained by Ecker et al [11] is evaluated in this work with respect to dose deviations. Ecker et al. trained two neural networks with a cohort of 78 fractions. One network is a commonly used architecture for medical image segmentation a 2-dimensional U-NET. The other network is based on a U-NET derived architecture as a 3D UNETransformer (UNETR) and uses MRI volumes as input. Ecker et al. used a TPS research plugin to generate a ground truth structure from the previously reconstructed applicator model, which was used as a basis for comparison. To evaluate a fully automated registration workflow, the NN-predicted applicator segmentations were used for rigid image registration with the best performing algorithm. To evaluate the segmentation and registration performance, the DICE coefficient and the mean distance error between dwell positions (MDE) were used. For a test cohort of 10 patients (20 fractions) Ecker et al. found a mean DICE coefficient of 0.70 ± 0.07 for the predicted applicator segmentations on the test set using UNETR. The registration scripts were written using the Python implementation of the Insight Toolkit (ITK) (Kitware, Clifton Park, NY) [58]. The ITK implementation of elastix [46] was used with default parameters. The workflow resulted in a mean MDE error of 2.7 ± 1.4 mm (with the NN predicted structures), and 0.7 ± 0.5 mm with the ground-truth structures. [11].

The aim of this work is to investigate the effects of this metric error of 2.7 ± 1.4 mm on the dosimetric deviation in relation to the interfraction variations. The question is whether 2.7 ± 1.4 mm is sufficient for a dosimetric evaluation and what effects the ground truth segmentation with an MDE of 0.7 ± 0.5 mm already has.

3. METHODS

3.1 Patient Cohort

As part of a research project at the Medical University of Vienna, a cohort of patient data was collected for study purposes. Nine patients (N=9) were treated at Department of Radiation Oncology of the AKH /MUW, with multiple sets of MRIs acquired at the time of planning and before and after irradiation of the planned fraction. For these patients, anatomical variations were expected due to the clinical experience of the treatment team, and therefore represent a biased cohort. The timing of the acquisitions and the nomenclature used in the work is shown in Fig. 13. Thus, there is always one MR on the planning day (*MRplan*) and two control MRs (*MRpre* and *MRpost*). To anonymize the study data, each patient's data was assigned a sequential case number: *EVIMR00*. . The cases were prepared for analysis as a comparison dataset of 18 cases (nine datasets from the *MRpre* and nine datasets from the *MRpost*).

For each MR image, three T2-weighted image series (para-transverse, sagittal, coronal) were acquired sequentially. Planning was always performed in the transverse plane. The MR device used was a Siemens open scanner (Magnetom C!, 0.35T, TSE, TR: 3290 ms, TE: 100 ms).

For all cases, the OAR structures were drawn by a radiation oncologist in the commercial TPS Oncentra® Brachy. All structures were contoured by the same radiation oncologist to avoid inter-observer variation. The structure set of the OAR was used equally for all registration methods. Evaluation was performed for the bladder, rectum, bowel and sigmoid.

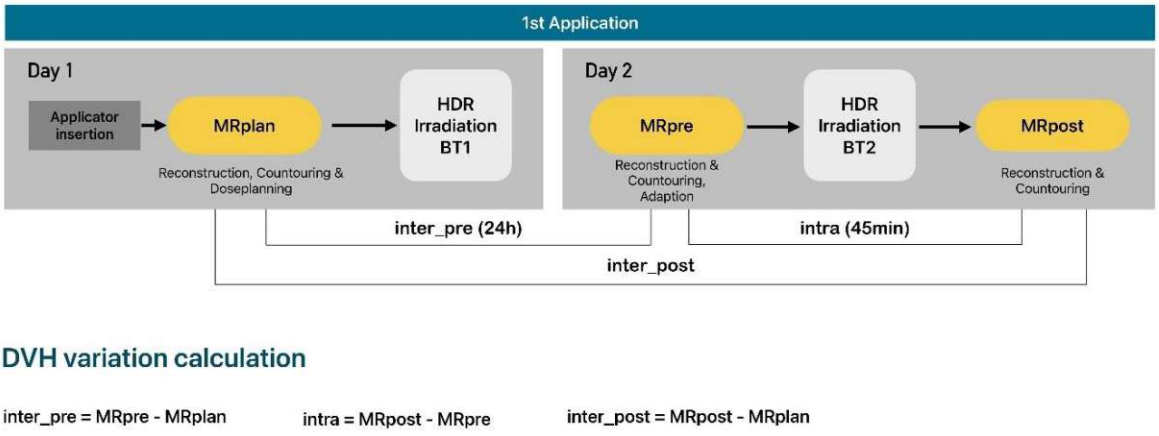

Fig. 13 Time schedule setup of the individual MR images of the study and nomenclature

3.2 Rigid applicator-based image registration in Ocentra® Brachy

The entire contouring of the OAR, the reconstruction of the applicator, the registration and generation of DVH parameters for landmark-based manual applicator-based registration took place in the TPS Oncentra® Brachy. Fig. 14 shows the steps required to perform the dosimetric evaluation for the control time using rigid landmark-based registration within a single case. The individual steps are described in the following chapters. This method will be referred to as *manual registration*.

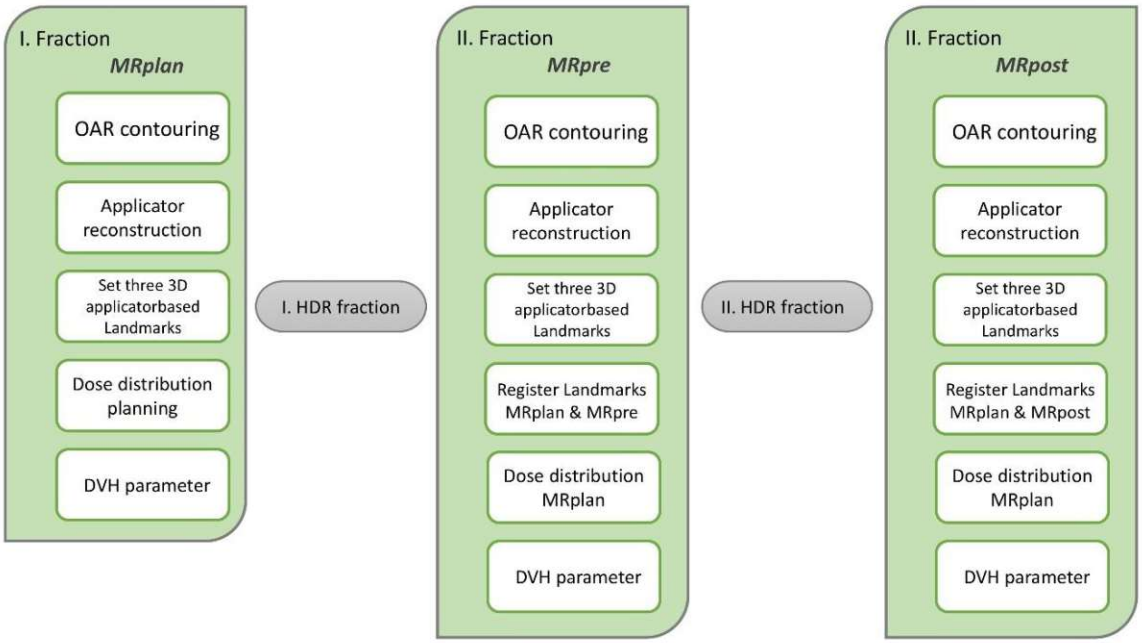

Fig. 14 Steps for the Landmark-based image registration

3.2.1 MANUAL PLACEMENT OF APPLICATORS FOR CONTROL MRI

To perform rigid applicator-based registration, the applicators had to be reconstructed in the image datasets from all time points. The applicator was placed on the MR image set of *MRplan*. This allows the medical physicist to determine the dose distribution prior to the first fraction and create a dose dataset. This *MRplan* dose dataset serves as a reference for the calculation of the interfraction variations for all investigated setups. For rigid applicator-based registration, the applicators were reconstructed in MRpre and MRpost as well. For all image sets, this reconstruction was performed as follows.

First, the image set was positioned in the TPS so that the applicator was approximately centered in the image and the tandem was vertical. The appropriate applicator model was then selected from the TPS library for the appropriate dimensions. In all cases discussed here, a Vienna Ring applicator was used. This model was positioned in the images based on the applicator and rotated accordingly. The tandem with the top of the applicator and prominent points in the ring, such as needle holes, serves as the main reference points (see Fig. 15).

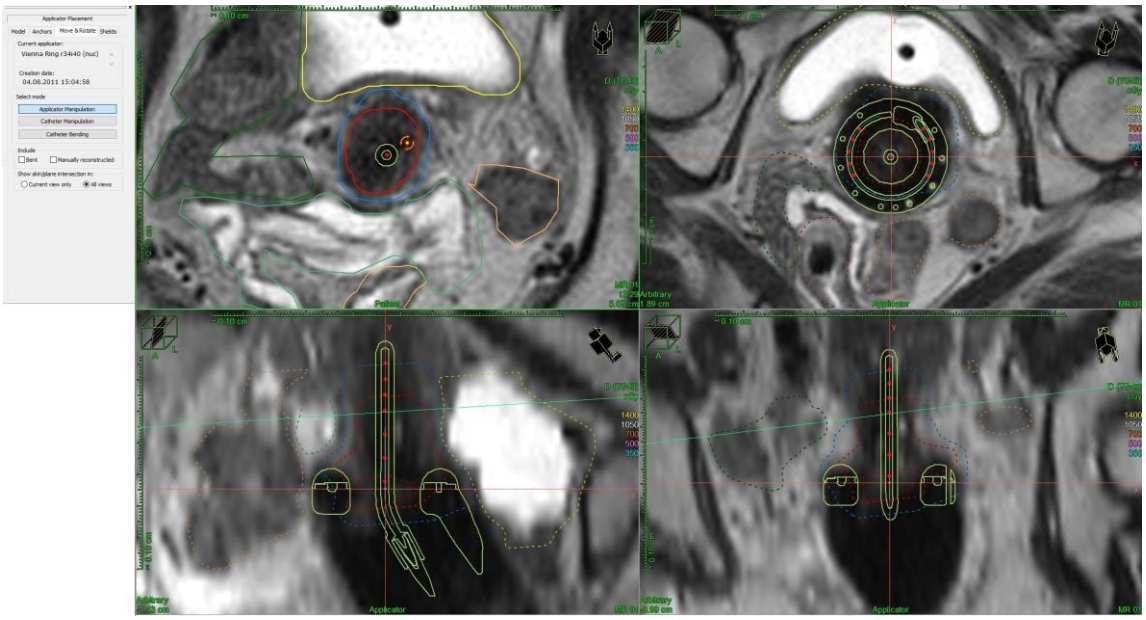

Fig. 15 Applicator placement according to visible applicator structures via translation and rotation in the TPS Oncentra® Brachy

3.2.2 LANDMARK-BASED IMAGE REGISTRATION

After reconstructing the applicators in the *MRplan* and in the control MR *(MRpre* and *MRpost*), it was possible to set landmarks. The TPS of Oncentra® Brachy calculates a sagittal and coronal image set from the para-transversal image data set. The TPS coordinate system was initially placed on the same prominent applicator lines from all perspectives of both cases. This can also be seen with the red coordinate system in the sagittal plane on Fig. 16. The center of the tandem and the two horizontal parts of the ring always served as orientation lines for the coordinate system axes. In the transverse plane, the z-axis was placed on a straight line of the ring model. With the coordinate system in place, the three equally selected applicator-based landmarks can now be set, as shown in Fig. 16. The exact layer at the coordinate origin of the z-axis of the sagittal plane was used. The first point was placed on the y-axis of the coordinate system at the intersection with the top of the applicator. The other two points were placed on the x-axis of the coordinate system, 2 cm to the left and 2 cm to the right of the origin. This procedure was repeated identically for the *MRplan* and the corresponding control MR (*MRpre* and *MRpost*). In addition, the coordinates of the landmarks were also noted.

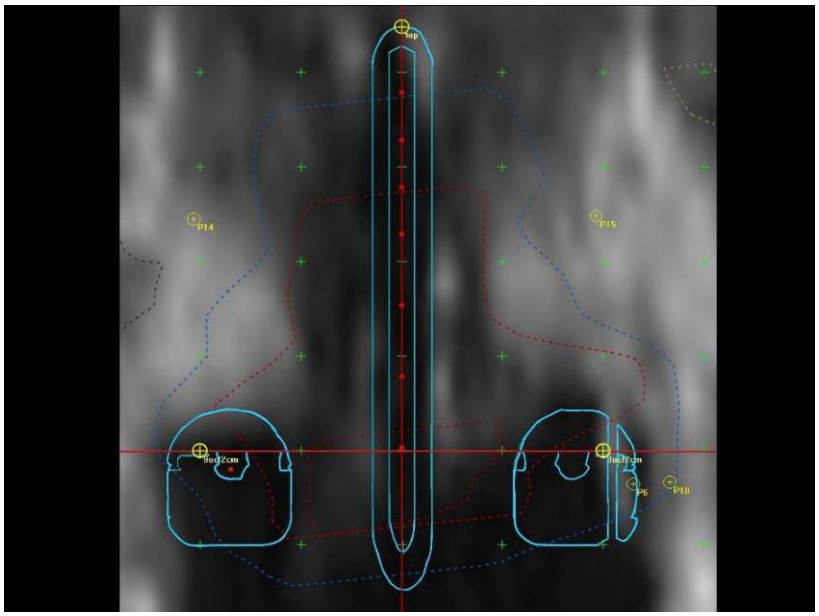

Fig. 16 Landmark positions in the sagital plane. One point on the y-axis of the coordinate system at the intersection with the top of the applicator. One point each on the x-axis of the coordinate system 2cm left and right of the coordinate origin. - Created in Oncentra® Brachy

To perform the registration, Oncentra® Brachy was used to create a separate registration case containing the transverse image sets of the images to be registered. In this case, the dose file from the planning and the structure set of the OAR from the control case were also added. The landmark coordinates of both image sets can then be entered into a table in the registration interface of the Oncentra® Brachy and a point matching algorithm registers the two image sets. During the registration of the control MR, the image parameters were adapted to those of the planning MR so that the coordinate system and the two applicators associated with the dose were superimposed. This allowed the dose distribution dataset to be transferred to the control MRs. After this step, the DVH for each organ could be calculated and put out in Oncentra® Brachy.

3.3 Applicator prediction

3.3.1 APPLICATOR-STUCTURE RECONSTRUCTION VIA ONCENTRA® BRACHY

Structure files of the applicator within DICOM form the basis for further registrations. A non-commercial research version of Oncentra® Brachy was used to generate a reference structure. This software includes a plug-in that creates a usable DICOM structure of the virtual 3D applicator model in Oncentra® Brachy. This was previously reconstructed manually in the MR set in Oncentra® Brachy for manual registration. The 3D applicator model was accurately translated into a DICOM structure. This was necessary because the structure of the applicator

was otherwise not included in the exported DICOM files. Based on this structure, the registration algorithm for the medical image processing and evaluation software Hero was able to perform a registration using the elastix toolbox (see chapter 3.4.2). This allows a comparison between the registration algorithms used - point matching algorithm and structure Euclidean distance map based registration. Since both use the same reconstruction of the applicator, this structure registration forms the ground-truth segmentation for the Hero evaluation.

The resulting structure will be referred to in the following with the nomenclature *Applicator Structure (AS)* [ground-truth segmentations] and all values referring to it will be labelled with the index ***AS***.

3.3.2 AUTOMATED APPLICATOR RECONSTRUCTION USING NEURAL NETWORK

To reconstruct the applicator using AI, all images were converted from DICOM format to NifTi .nii format (for easier handling and processing of the image data) and scaled to the same shape of images per MR image set. Most of the MR data sets contained 30 slices, and were brought to a shape of 32, since the neural network needs a number divisible by 16. It was important to keep the orientation, position, and voxel size of the image. After completing the preliminary work, the image sets were run through the 3D UNETR network of Ecker et al. [11]. The output was in NifTi format as an image set for the MR and an image set for the reconstructed applicator.

All values related to the resulting applicator prediction by the neural network [predicted segmentations] were labelled with the index ***AI.***

3.4 Evaluation in the Hero-Toolkit

The interfraction variations of the neural network generated applicator prediction was analyzed in Hero (Hero Imaging 2022). Hero is a medical image processing and analysis software. Hero uses the Insight Toolkit (ITK) [58], the gold standard medical image analysis software library, and Elastix [46] to perform mathematical operations and image processing [45]. For image visualization, Hero uses a module based on the open source Visualization Toolkit [59]. It offers the possibility to create visual analysis scripts with the help of operating elements.

The AS was created to transfer the virtual applicator model from Oncentra® Brachy for evaluation in Hero. This also makes it possible to compare and evaluate the generation of DVH parameters and registration methods in Hero and the evaluation in Oncentra® Brachy, as both programs are based on the same applicator reconstruction.

At the same time, registration was also performed based on the AI-based applicator reconstruction in Hero. This allowed DVH parameter analysis and a comparison of interfraction variations between the two methods.

The individual steps are discussed in more detail in the following sections.

3.4.1 DICE COEFFICIENT

Based on the 9 x 3 MR images of the study, the predictive accuracy of the neural network was calculated using the DICE coefficient and compared with the work of Ecker et al [11]. The coefficient measures the overlap between the two structures and provides a value between 0 and 1, with a value of 1 representing a perfect match.

$$DICE = \frac{2|X \cap Y|}{|X| + |Y|} \tag{3}$$

X symbolizes the AS of the applicator and Y are the mask values of the AI prediction.

A Hero script was used to compare the AS predicted by Oncentra® Brachy with the structure generated by the neural network and calculate the DICE coefficient.

3.4.2 HERO-TOOLKIT SCRIPT

Two DVH data sets of the DVH parameter have now been generated using the Hero script for the registration process. The description of the DVH parameter generation is shown in this chapter. One dataset was based on the applicator structures (AS) generated by the Oncentra® Brachy plug-in. All parameters derived from this dataset were labelled as *AS-based*. The other dataset was based on the applicator predictions generated by the neural network. The parameters derived from this dataset were labelled *AI-based*.

To be able to register the respective images, masks had to be created in Hero from the AS-based structure file containing the applicator contour.

For AI-based registration, the NifTi applicator prediction image set was converted to a mask using the Threshold function. The results were fed into the registration algorithm.

For registration, the mask of the applicators of the images to be registered was overlaid with a filter, that fills small holes and irregularities of the applicator mask. Subsequently, a Euclidean distance map was generated from this mask. Each voxel value in the resulting image represents the Euclidean distance to the nearest edge voxel in the mask. Distance maps from the two applicators can be registered to each other using the Elastix toolbox. Using the transformation matrix obtained for the image set to be moved, the image and contours were converted to their new coordinates.

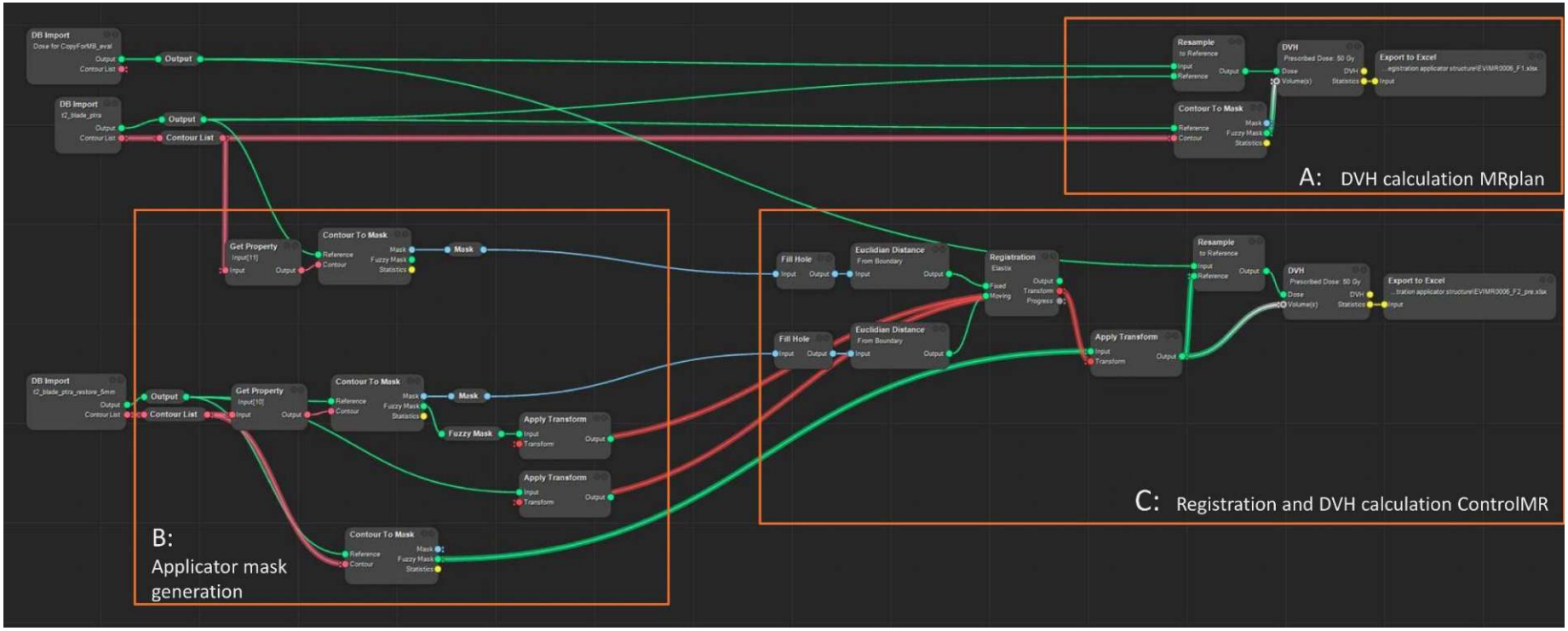

Fig. 17 Hero script for registration and calculation of DVH parameters for AS-based registration. DICOMs for planning and control MR as well as the dose file are given as input. A: Using "Contour to Mask", all OAR contours are converted to masks while the dose is resampled to the DICOM MRplan. The DVH for MRplan can now be calculated from both. B: The applicator structure is read from both DICOMs (MRplan and ControlMR [MRpre or MRpost]) using "Get Property" and converted into a mask using "Contour to Mask". C: "Fill Hole" is used to compensate for errors in the applicator mask and an Euclidian distance map is then created. These two distance maps are registered using the Elastix Toolbox. The transform parameters are transferred to the OAR masks of the ControlMR using "Apply Transform". The DVH of the ControlMR can now be calculated using the resampled dose and the transformed OAR. - Created in Hero

Once the image characteristics of the dose were matched to those of the control MR, and the dose and contours were used to calculate the DVH with the volume and D_2 of each organ.

The Hero script for the registration and calculation of the DVH parameters is shown with the conversion of the *AS* DICOMs into a mask in Fig. 17.

3.5 Report inter- and intrafraction DVH variations

As an additional analysis to the DICE coefficient, the reference value of the rigid manual method for each individual dose parameter was subtracted from the DVH data generated from the different registrations before calculating the interfraction variations. This makes it possible to determine the direct influence of the automated registration methods on the calculation of the DVH parameters. The mean dosimetric deviation was calculated from these values and is presented in chapter 4.2.

An Excel script was used to evaluate the inter- and intra-fraction variations. First, the volume, $D_{0.1cm^3}$ and D_{2cm^3} for the bladder, rectum, sigmoid and bowel, were extracted for each case from the DVH generated by Oncentra® Brachy or Hero. In addition, the absorbed dose was converted to EQD2. Calculation of inter- and intra-fraction variations was performed for volume, D_{2cm^3} and EQD2 according to the scheme described in Fig. 13 with the following calculation:

$$\begin{aligned} inter\_pre &= MRpre - MRplan \\ inter\_post &= MRpost - MRplan \\ intra &= MRpost - MRpre \end{aligned} \qquad (4)$$

The DVH evaluation of inter- and intra-fractional variations was performed for all three different registration methods. This results in one inter- and intrafraction variation data set for manual registration, one for AS-based registration and one for AI-based registration. As a reference dataset, the manual registration data was used to quantify the inter- and intra-fraction motion of the patient cohort.

To analyze the dosimetric registration inaccuracy of each method, the D_2 and EQD2 values for each organ were compared between manual registration and AS-based or AI-based registration. For this purpose, each intra- or interfraction dose parameter calculated with the manual registration method was subtracted with the corresponding intra- or interfraction parameter from the AS-based or AI-based registration method. This resulted in two sets of

difference data, one for AS-based and one for the AI-based registration. The calculation of differences is shown in Fig. 18.

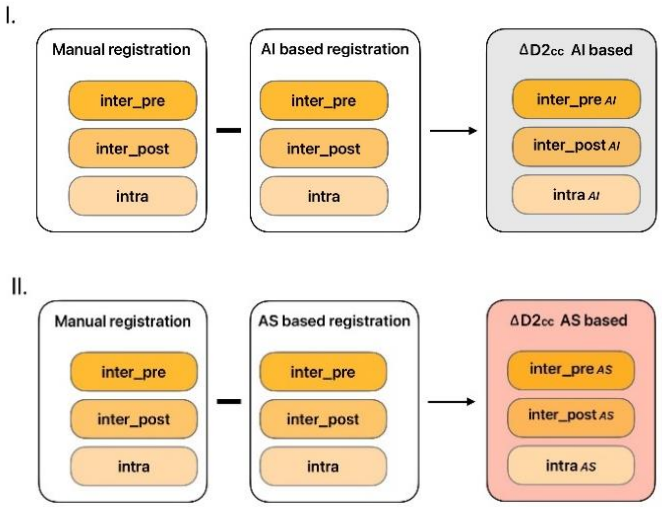

Fig. 18 Calculation schedule setup for the dosimetric inter- and intrafraction variation differences between the manual registration method and I. the AI-based and II. the AS-based registration method.

To test the significance of the data, a one-sided paired samples t-test with dependent samples was performed between the AS-based and AI-based difference data for the bladder, rectum, sigmoid and bowel organs. A significance level of 0.05 was used.

4. RESULTS

4.1 Clinical interfraction variation results

The results for the planned fraction showed a mean volume of mean (M)=138.55 cm³ (SD=63.09 cm³) for the bladder and a mean absorbed dose of M=5.22 Gy (SD=0.69 Gy , giving a mean of M=8.67 Gy_{EQD2} (SD=1.98 Gy_{EQD2}) converted to EQD2. For the rectum, the mean volume was M=49.38 cm³ (SD=15.60 cm³), the mean dose was M=2.92 Gy (SD=0.97 Gy) and converted to EQD2 a dose of M=3.63 Gy_{EQD2} (SD=1.75 Gy_{EQD2}). For the sigmoid, the mean volume was M=78.68cm³ (SD=28.43 cm³), the mean dose was M=3.47 Gy (SD=0.63 Gy) and converted to , the dose was M=4.56 Gy_{EQD2} (SD=1.23 Gy_{EQD2}). The bowel had a mean volume M=150.16 cm³ (SD=140.04 cm³), a mean dose M=1.95 Gy (SD=1.44 Gy) and converted to EQD2 a dose of M=2.30 Gy_{EQD2} (SD=2.22 Gy_{EQD2}). All raw data for manual registration are presented in Table 7. Data for AS-based registration can be found Table 6 and data for AI-based registration is given in Table 8.

Table 4 Dosimetric variations for D_{2cm^3} bladder, rectum, sigmoid and bowel. Mean M differences, SD standard deviations, minimum (Min), maximum (Max) and median (Med) values for different time intervals.

Interfraction pre in Gy_{EQD2}

	Mean	SD	Min	Max	Med
Bladder	0.9	2.0	-3.1	3.6	1.2
Rectum	-0.3	1.4	-2.4	2.4	0.0
Sigmoid	0.8	2.4	-2.0	4.6	0.7
Bowel	0.2	2.5	-5.0	4.9	0.3

Intrafraction in Gy_{EQD2}

	Mean	SD	Min	Max	Med
Bladder	1.0	2.8	-3.0	5.7	0.3
Rectum	-0.3	1.1	-3.0	0.5	0.0
Sigmoid	-0.2	1.9	-3.6	3.1	0.2
Bowel	-0.2	1.7	-3.3	3.0	-0.1

Interfraction post in Gy_{EQD2}

	Mean	SD	Min	Max	Med
Bladder	1.9	2.6	-2.0	7.1	1.8
Rectum	-0.5	1.8	-3.3	2.9	-0.2
Sigmoid	0.6	2.4	-3.6	4.9	0.6
Bowel	0.0	2.1	-3.9	4.0	0.1

To define a ground truth for the interfraction variations, the interfraction variations resulting from the calculation of the manual registration method were first analyzed. The results for the

volume changes are shown in Fig. 29 while the corresponding EQD2 dose change is shown in Fig. 19 and Table 4.

In the cases examined here, it can be seen that the volume differences between the individual examination points for the bladder (M=39%, SD=60%), rectum (M=-9%, SD=41%) and sigmoid (M=22%, SD=33%) were much smaller than for the bowel (M=83%, SD=197%). For the bladder, patient EVIMR0006 shows particular anomalies (compare Fig. 27 and Fig. 9). In this case, the bladder grows by 73% between the first and the beginning of the second fraction and by another 105% during the second fraction. In total, it increased by 408.6 cm³. This change was also reflected in the dose range. In this case there was a change of 3.1 Gy_{EQD2} for the inter_pre, a change of 4.0 Gy_{EQD2} for the intra and a change of 7.1 Gy_{EQD2} for the inter_post. In addition, in patient EVIMR0004 there was a bladder increase of 131% for inter_post. However, this was not reflected dosimetrically. Also, in the EVIMR0001 case, the bladder grows by 83% between the first fraction and the start of the second fraction, which also had a dosimetric effect (inter_pre = 3.6 Gy_{EQD2}). During the second fraction, the volume decreases by 38%, which again results in a dose change (intrafraction = -3.0 Gy_{EQD2}).

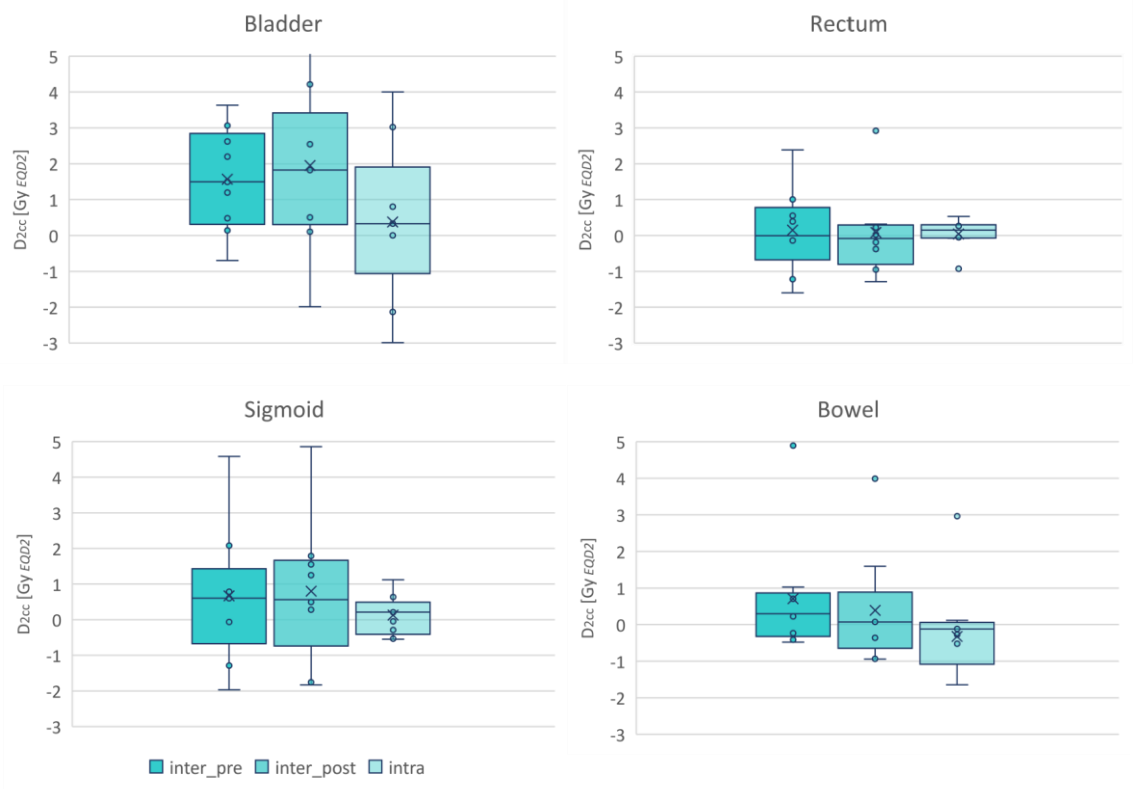

Fig. 19 Inter- and intrafraction variation of the manual registration in Gy_{EQD2}

In the rectum, striking deviations were detected especially for case EVIMR0008. Here, the volume first increases by 101% between fractions and shifts upwards into the dose-relevant range, so that the dose impact for the inter_pre increases by 2.4 Gy_{EQD2}. The volume then decreased by a further 18% during the second fraction. However, the dose effect increased by

0.5 Gy_{EQD2}. For the EVIMR0010 post case only one rectum layer was visible, so no volume was measured for this case.

In the sigmoid region, the overall dose input was much lower than for bladder and rectum. Thus, volume changes have a smaller absolute effect on the dose here. Case EVIMR0006 was a special example. Here the volume changed by 58% from the first fraction to the beginning of the second fraction, resulting in a dosimetric difference of 4.6 Gy_{EQD2}. The increase of the volume for the inter_pre of the cases EVIMR0005 (60%) and EVIMR0007 (53%) had only small dosimetric effects.

In the bowel, the reported volumes varied widely between patients, ranging from 7.39 cm^3 to 432.74 cm^3. Thus, there were very large volume differences between the fractions and the relative volumes, as well as within the dose values. This was particularly striking for the cases EVIMR0004 and EVIMR0005. For case EVIMR0004, the volume between the first and second fraction increases by 548%. This, however, produces a dose difference of just 0.3 Gy_{EQD2}. In case EVIMR0005 the volume for inter_pre even increased by 776%, also resulting in a dose difference of 4.9 Gy_{EQD2}. However, despite the small volume change of -38%, the dose decreased again by 3.3 Gy_{EQD2} in the second fraction and therefore was outside the clinically relevant range.

Further observations were made during the intrafraction period to see if there was a dosage trend with longer treatment times. The mean treatment time between the two MRIs was determined to be 46 min. The results were analyzed; however, no clear pattern was identified. A detailed graph is shown in Appendix Fig. 31.

4.2 Consistency of used software and registration deviation

The mean DICE coefficient of the predicted applicator structures was 0.67 ±0.09.

The mean dosimetric deviation resulting from the registration differences in Hero compared to Ocentra is listed in this section. For each individual dose parameter, the reference value of the rigid manual method was subtracted from the DVH data generated from the different structures in Hero. For the AS-based registration, it was found that the mean dose values for the bladder (M=0.4 Gy_{EQD2}, SD=0.6 Gy_{EQD2}), rectum (M=0.3 Gy_{EQD2}, SD=0.1 Gy_{EQD2}), sigmoid (M=0.3 Gy_{EQD2}, SD=0.3 Gy_{EQD2}) and bowel (M=0.2 Gy_{EQD2}, SD=0.2 Gy_{EQD2}) changed with the use of Hero compared to manual registration.

For the AI-based registration, the dosimetric registration inaccuracy of the bladder was (M=0.2 Gy_{EQD2}, SD=2.0 Gy_{EQD2}), rectum (M=0.3 Gy_{EQD2}, SD=0.8 Gy_{EQD2}), sigmoid (M=-1.2 Gy_{EQD2}, SD=5.0 Gy_{EQD2}) and bowel (M=0.2 Gy_{EQD2}, SD=0.5 Gy_{EQD2}) compared to manual registration.

4.3 Interfraction dose difference

In this chapter, the differences in inter- and intrafraction variations between the three registration methods considered in this work were presented. According to Fig. 18, the results of the Δ D_{2cm^3} inter- and intrafraction variations of I. AI-based reconstruction and II. AS-based registration in Hero were compared with those of manual registration in the Oncentra® Brachy (benchmark). The results for the absorbed dose deviation are shown in Fig. 20 as absolute dose in Gy and in Fig. 21 in relative form. The deviation of the equieffective biological dose equivalent is shown as absolute dose in Gy_{EQD2} in Fig. 22 and in relative terms in Fig. 23.

Looking at the results of the four plots, several correlations can be identified. For all rectum and bowel results, the mean and median values of the individual box plots were close to the zero line. This applies to both AI-based and the AS-based differences. For rectum, the median and mean were ± 0.1 Gy (± 8%) and ± 0.3 Gy_{EQD2} (± 12%), respectively. The values for the bowel were also similar at ± 0.1 Gy (± 11%) and ± 0.3 Gy_{EQD2} (± 14%). For AS-based boxplots of the bladder, the mean and median values of the individual boxplots were also close to the zero line. However, both were clearly in the negative range for the $inter\_pre_{AI}$ in all plots. An exception for organs were the results of the AI-based inter- and intrafraction variation differences for the sigmoid. These were essentially more negative, especially in the mean, than those of the AS-based reconstruction. For the presentation of the absorbed and absolute dose difference of the sigmoid in Fig. 20. This means a mean for $inter\_pre_{AI}$ of -0.3 Gy and a median of -0.2 Gy. For the $inter\_post_{AI}$ and the $intra_{AI}$, the median were very close to zero, but the means were -0.5 Gy and -0.3 Gy. The mean of the $inter\_post_{AI}$ stands out with -14 % shown in the relative representation in Fig. 21. This difference between the AI-based and AS-based values was also evident in the EQD2 dose difference plot and the absolute sigmoid in Fig. 22. In this case the mean was -1 Gy_{EQD2} for $inter\_pre_{AI}$, -2.2 Gy_{EQD2} for $inter\_post_{AI}$ and -1.2 Gy_{EQD2} for $intra_{AI}$. In relative terms (Fig. 23) it can be seen that the mean for the $inter\_pre_{AI}$ was -26 %, whereby the $inter\_pre_{AS}$ was -11 % as well. The mean and median of the intrafraction were very similar for both, while the mean of the $inter\_post_{AI}$ was -45 %.

Furthermore, a general observation of all diagrams was that the Interquartile range (IQR) of the boxes was much wider for the AI-based boxes than for the AS-based boxes. An exception to this are the relative boxes of the bowel interfraction variations in Fig. 21 & Fig. 23 of the applicator structure (AS). The latter have a very high width and were therefore as wide as those of the AI. For the bladder and sigmoid colon, the dose differences were essentially higher than for the rectum and bowel.

For the significance test, it was found that the differences in the inter- and intrafraction variations of the AI-based method for all OARs in relation to the AS-based method could not be considered significant. The corresponding values can be found in the Table 9 in the appendix.

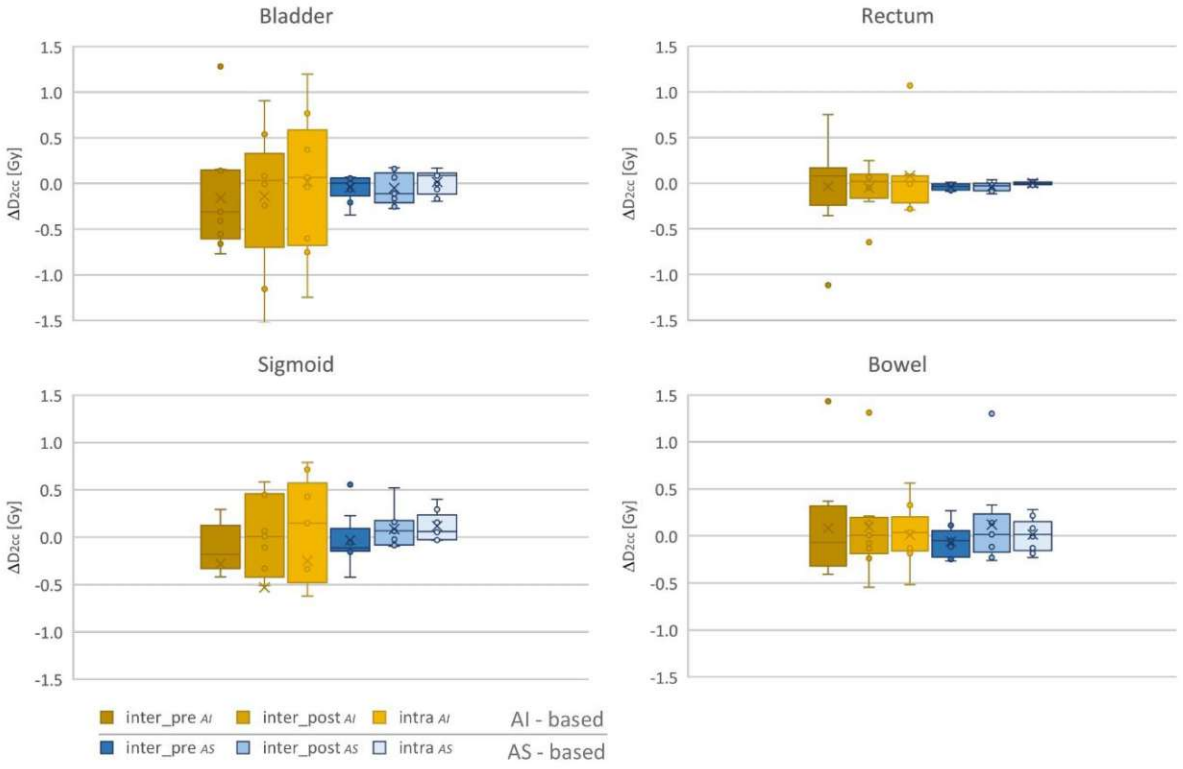

Fig. 20 Difference between inter- and intrafraction dose variations in manual registration and automatic registration based on I. AI reconstruction and II. the AS in Gy (Outliers: Sigmoid inter_pre$_{AI}$= -1.93 Gy, inter_post$_{AI}$= -5.4 Gy and the intra$_{AI}$= -3.48 Gy)

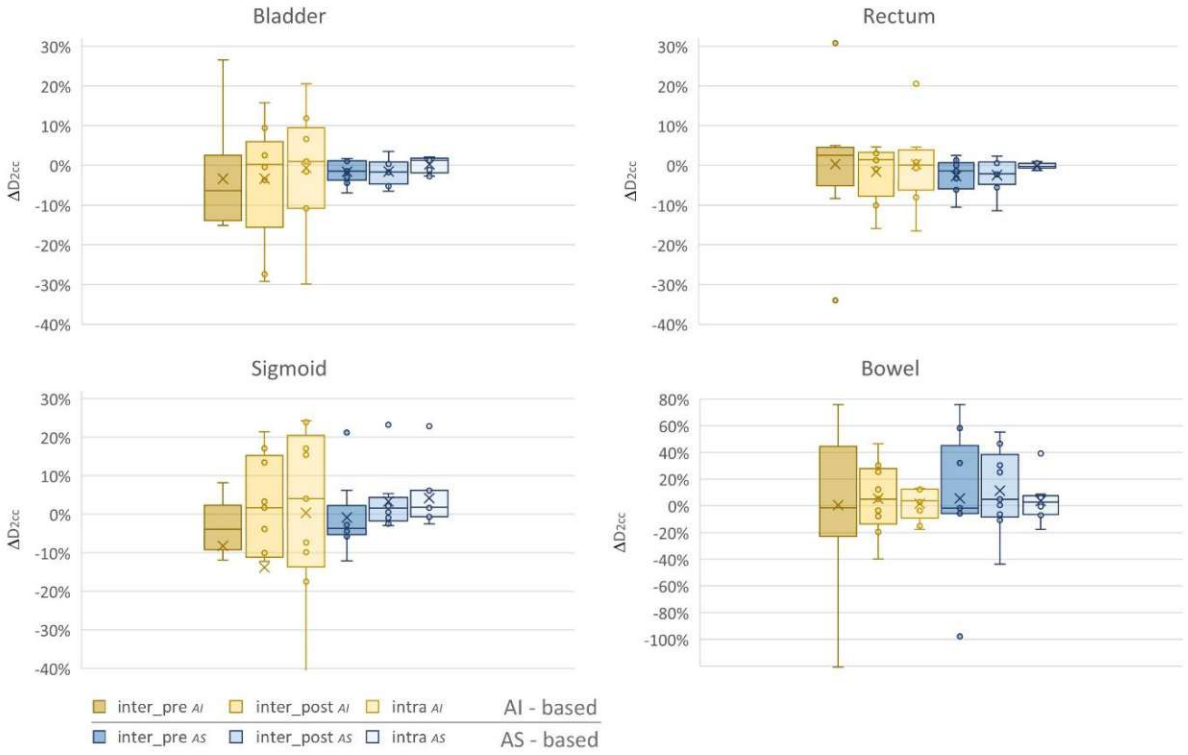

Fig. 21 Difference between inter- and intrafraction dose variations in manual registration and automatic registration based on I. AI reconstruction and II. the AS in % (Outliers: Sigmoid inter_post$_{AI}$= -155 %)

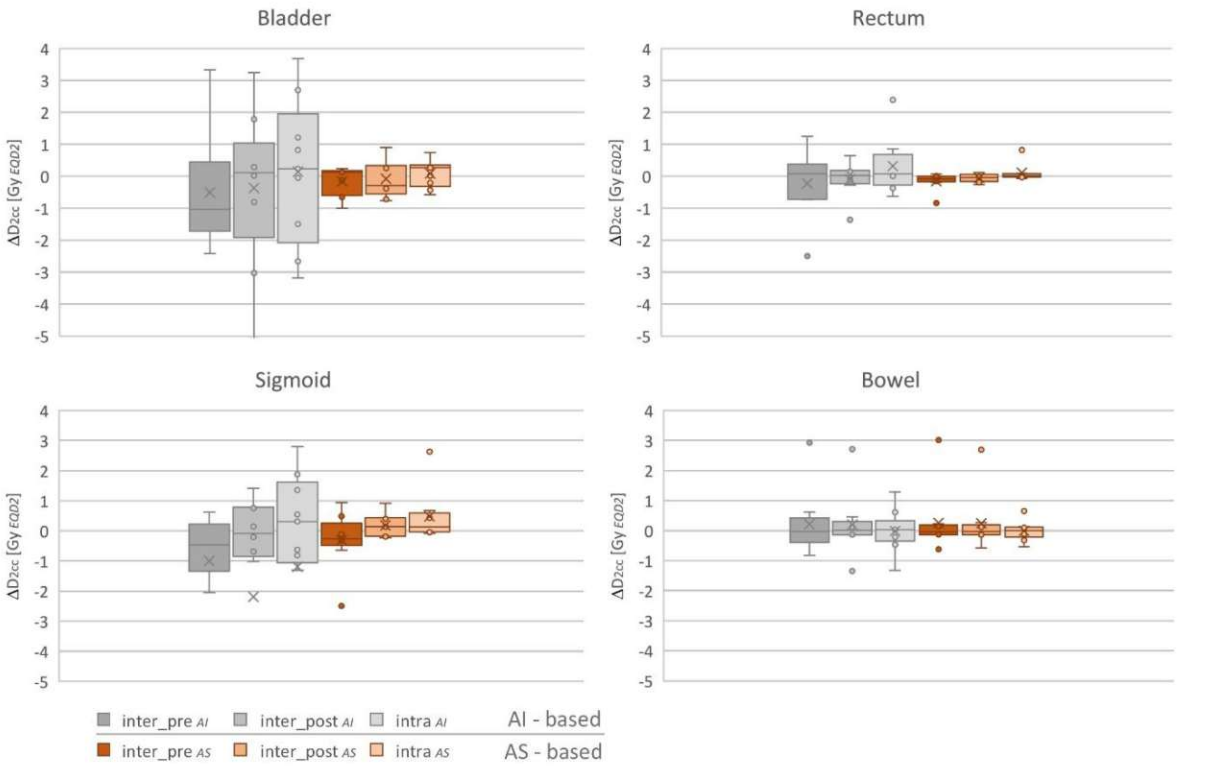

Fig. 22 Difference between inter- and intrafraction dose (EQD2) variations in manual registration and automatic registration based on I. AI reconstruction and II. the AS in Gy_{EQD2} (Outliers: Sigmoid $inter\_pre_{AI}$= -5.93, $inter\_post_{AI}$= -20.83 and $intra_{AI}$= -14.9)

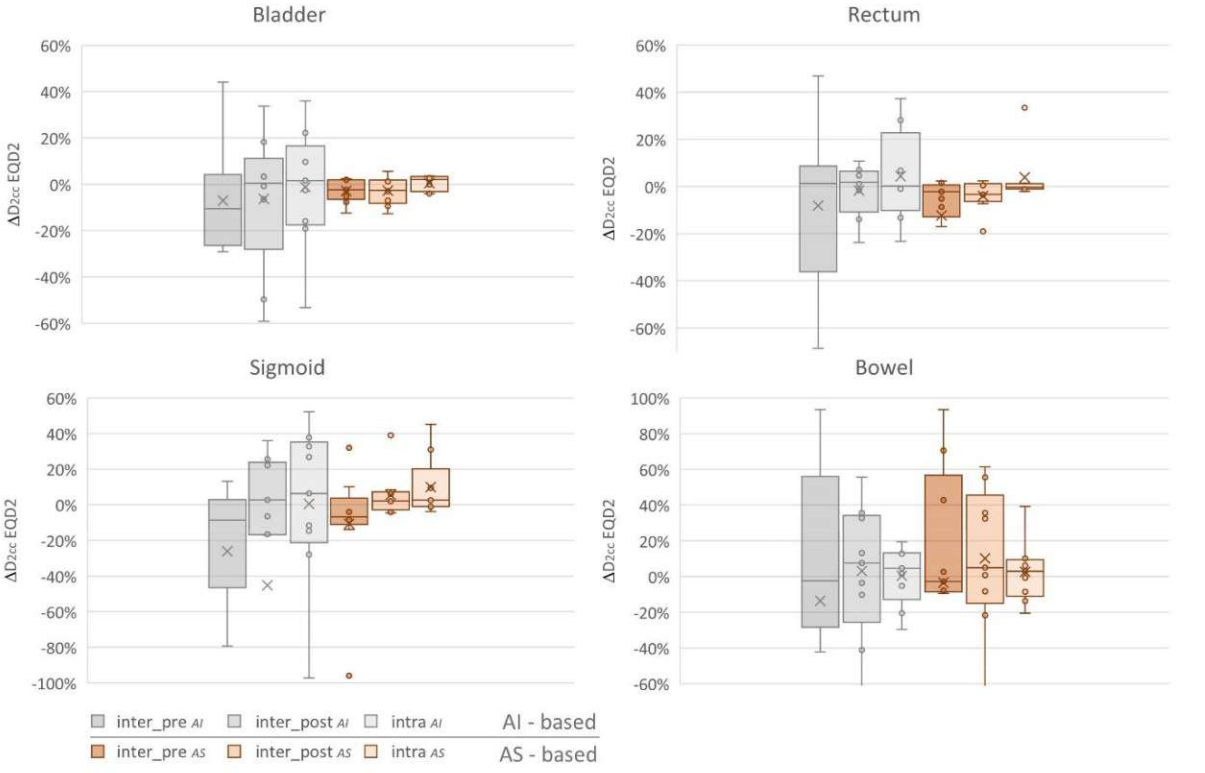

Fig. 23 Difference between inter- and intrafraction dose (EQD2) variations in manual registration and automatic registration based on I. AI reconstruction and II. the AS in % (Outliers: Sigmoid: $inter\_pre_{AI}$= -135 %, $inter\_post_{AI}$= -456 % ; Bowel: $inter\_pre_{AI}$= -280 %)

5. DISCUSSION

To discuss these study results, it is necessary to emphasize that the selection of patients in the study was not random. However, it can be stated that the subjects were selected based on possible organ variations. This assumption is borne out in some cases with large shifts and interfraction variations in both OAR volumes and dose. The selection of subjects particularly affects the clinical evaluation of interfraction variations and the comparison with the literature.

The evaluation of the significance test for the differences in the inter- and intra-fractional variations of the different registration types did not show a clear trend. Therefore, the significance test does not confirm an inevitable systemic deterioration of the data in the AI-based registration compared to the AS-based registration. The sample size is probably too small to determine a statistically significant effect. Nevertheless, the plots clearly show that there are deficits. The available results of these data are classified below.

5.1 Clinical interfraction variation result discussion

To classify the results of the clinical inter- and intrafraction variance obtained here, a comparison with the literature should be made first. Comparing the inter_pre results obtained here from Table 4 with those of Nomden et al. [38] (Table 3), it can be seen that the mean dose deviations differ from those of Nomden et al. [38] by several tenths of a Gy_{EQD2}. For the bladder and sigmoid, the mean increased by 0.8 Gy_{EQD2} and 0.4 Gy_{EQD2}, respectively. For the rectum, however, it decreased by -0.7 Gy_{EQD2}.

In terms of the inter_post, the difference between the results of Nomden et al. and those of this work is particularly pronounced for the bladder mean of 2.1 Gy_{EQD2}. The sigmoid was 0.5 Gy_{EQD2} higher, while the rectum had a mean of -0.2 Gy_{EQD2} less. For the intrafraction, the mean difference was 1.1 Gy_{EQD2} for the bladder, -0.2 Gy_{EQD2} for the rectum and -0.1 Gy_{EQD2} for the sigmoid. These differences highlight that at each time point the bladder (D_{2cm^3} mean) received more dose in the second fraction compared to the first fraction, which differs from the results of Nomden et al. Conversely, the rectum received less dose (M) in the second fraction compared to the first fraction than in Nomden et al. [38].

However, the SD of the results of Nomden et al. are higher for all organs at all time points in the present study. These results may be due to the fact that Nomden et al. treated 30 subjects continuously in their study, whereas this study only treated nine subjects plus a selected cohort. This could have an influence on the dispersion of inter- and intrafraction variations.

The random SD in Nesvacil et al [10] of interapplication in the physical dose to the bladder was ±21.2%, while ours was ±11% for inter_pre and ±18% for inter_post. The SD of the

intrafraction was ±17.7% while in our case it was only ±13%. This means that the random SD and thus the dispersion of the dose deviations for the bladder in our study is lower than in Nesvacil et al. [10].

For the rectum, the random SD of the interapplication found by Nesvacil et al. [10] was ±22.8%. This inter_pre was ±28% and inter_post was ±32%, which is several times higher. In other words, rectal variations were more common in our study. The SD of the intrafraction was ±20.5%, whereas the interfraction was only ±7%, which is lower than shown by Nesvacil et al. This means that the bladder and rectum in our cohort had less random interfraction variation or some with less variation. This result could also be influenced by patient selection.

Sigmoid and bowel were combined in Nesvacil et al. and the random SD of the interapplication was determined to be ±30.2%. In our results the inter_pre and inter_post was ±26% and ±28% for sigmoid and ±85% and ±43% for bowel. These high standard deviations are due to the high number of outliers in EVIMR0005. On the other hand, there are strong outliers in our cohort for the bowel and sigmoid region, which drive up the SD. This is the reason for the difference to Nesvacil et al. The SD of the intrafraction was ±23.5%, while ours was only ±9% for the sigmoid and ±23% for the bowel.

In the following section the outliers of the inter- and intrafraction variation of the individual organs will be discussed. For the bladder, case EVIMR0006 is suspicious. In this case the bladder volume increased clearly between fractions. As shown in Fig. 9 and Fig. 10, a dose increase is associated with a shift of the bladder wall and D_{2cm^3} into the an area of steeper dose gradients. The change in bladder volume caused a shift of the bladder wall towards the applicator, so that the bladder wall extends over the entire cranio-caudal length of the ventral tandem. In addition, the enlarged bladder will approach half the circumference of the applicator ring. These two circumstances result in higher D_{2cm^3}. In this case, it would be important to follow the bladder filling protocol and review the patient's overall treatment plan data to see if this change affects the overall Limits for Prescribed Dose for the bladder of <90 Gy_{EQD2}.

In the EVIMR0008 case, the rectal volume between the MRplan and MRpre increased by 101% and the inter_pre dose also increased by 2.4 Gy_{EQD2}. This results from a volume change in the superior/dorsal direction and D_{2cm^3}- relevant rectal wall shifted towards the applicator ring. This could be caused by gas in the rectum.

Case EVIMR0006 is also remarkable in terms of the sigmoid. Although the volume of the inter_post only changed by 58%, the growing bladder pushes the sigmoid into the dose-relevant range. This results in a dose change of the inter_post of 4.9 Gy_{EQD2} or 97%.

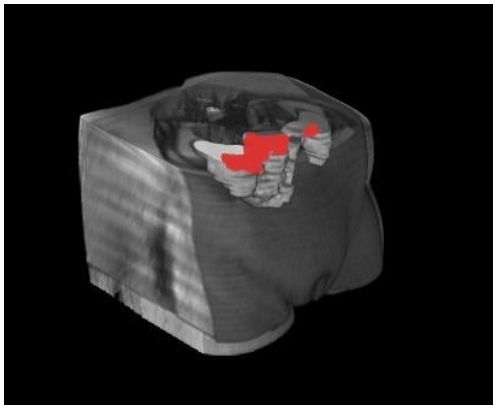

Fig. 24 Bowel volume EVIMR0005 MRplan (red) & MRpre (white) - created in Hero

Since intestinal loops in the abdomen are very flexible, the bowel and sigmoid loops may move near the brachytherapy applicator at different times. This can result in large variations of delineated organ volumes. An example of this can be seen in the MR0005 case (Fig. 24). In MRplan (red), only one bowel loop with a very small bowel volume is visible, far away from the applicator. In MRpre (white), the bowel volume is greatly enlarged and shifted (volume inter_pre = 776%) and enters the dose-relevant range with a bowel loop (inter_pre = 4.9 Gy_{EQD2}). In both MRs, a comparable area of the patient was scanned (with a cranial shift of about 5 mm between the two images, so that there is an additional contour layer over the uterus in the MRpre). All bowel loops visible in the field were marked on both images.

In addition, the D_{2cm^3} dose ranges for sigmoid and bowel are often divided into several fields of the organ wall, which can lead to significant dose changes.

5.2 Consideration of AI-based reconstruction uncertainty and impact on registration

The evaluation of the reconstruction accuracy of the applicator by the neural network shows that the DICE coefficient of 0.67 ±0.09 is almost identical to that of Ecker et al [11] of 0.7 ±0.07. This result shows that the network appears to be consistent, but still has room for improvement. In most cases, the reconstruction of the applicator by the AI works quite well. However, there are still inaccuracies. The inaccuracy of the dice coefficient results from a segmentation error of the neural network. The segmentation error is based on the difference between the training applicator model and the models used in Oncentra® Brachy. While only the tandem and the ring are used in the training model, the tubes connected to the afterloader are also visible in the Oncentra® Brachy models (see Fig. 25). As can be seen in case EVIMR0010 clin (see Fig. 25), the network sometimes incorporates surrounding structures

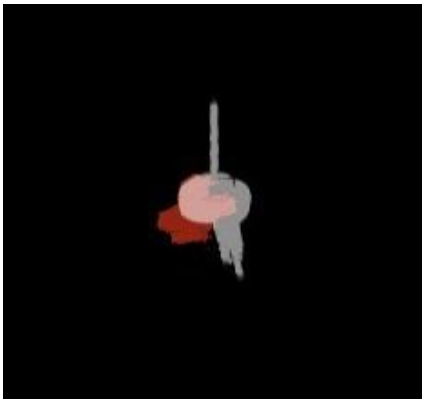

Fig. 25 Applicator prediction of the case EVIMR0010 clin: AI-based reconstruction (red) with included tumor parts and missing tandem & AS-based reconstruction (white) with connected tubes - created in Hero

such as the tumor into the applicator structure. As a result, the subsequent registration is inaccurate.

A further consideration regarding the origin of the different volumes and DVH of the organs is the distinction between the interpolation of volumes during the individual MR sequences in Oncentra® Brachy or Hero. This shows that the volume can be different for individual structures due to the calculation. Kirisits et al. [36] investigated the difference for a standardized volume of a 4 mm CT scan in different planning systems in 2007. They found a deviation of up to 7%. For the comparison of Oncentra® Brachy and Hero, this comparison still has to be made. For example, the EVIMR0004 pre case shows, that the volume of the bowel in Oncentra® Brachy was calculated to be 47.90 cm^3, while in Hero it was only 36.13 cm^3. In this case, the effect on D_{2cm^3} at doses of 0.61 Gy_{EQD2} and 0.43 Gy_{EQD2} is very small because the dose to the bowel in this case is very low. According to Kirisits et al [36], there may also be differences in the calculation of DVH between different planning systems. They found a difference of up to 5% for D_{2cm^3}.

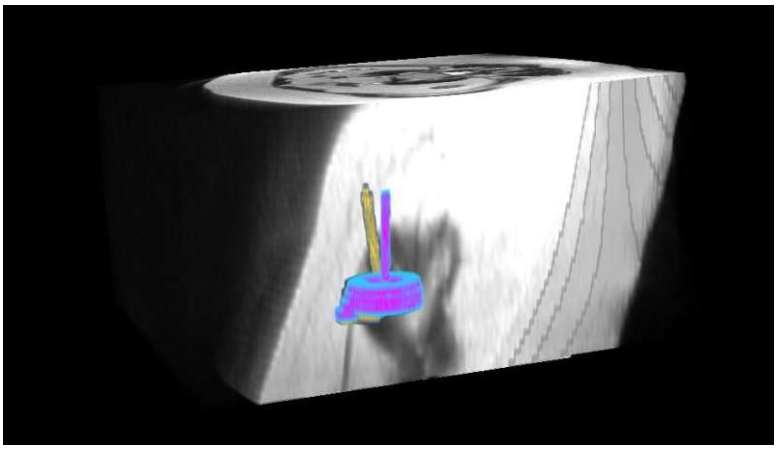

Fig. 26 Registration error EVIMR0006 between EVIMR0006 post (yellow) & EVIMR0006 clin (violet) after AS based reconstruction. In this case, poorly executed registration. - created in Hero

In some cases, the registration algorithms also fail by large, despite an excellent applicator reconstruction being available (see Fig. 25.). Consequently, this can lead to an elevation of interfraction variations reported based on these image registrations. Tanderup et al. [44] investigated the dosimetric effect of geometric uncertainties in the applicator position (e.g. when reconstructing with or without image registration). This group showed that the influence of small shifts in applicator reconstruction on dose is relatively small. They found that the most sensitive organs were the rectum and bladder, where mean D_{2cm^3} shifts were 5-6% per mm of applicator displacement in the anterior-posterior direction, and less than 4% for other organs and directions [44]. In the context of this work this means that small applicator reconstruction uncertainties and small registration uncertainties would have a limited impact on reported doses. However, in cases where these geometrical uncertainties add up more than 2-3mm, reported doses are largely affected by uncertainties in the method and consequentially reported interfraction variations would become unreliable.

5.3 Evaluation of the interfraction dose difference

The main question of the present work is whether the AI algorithm is sufficient to provide an estimate of the dosimetric inter- and intrafraction variations of the OAR. For this purpose, a ground truth evaluation of the dosimetric influence was first performed with the AS-based registration. Of course, this method also has a registration error compared to the manual registration in the Ocentra. This already shows that the registration deviations have a different dosimetric influence on the individual OAR. For the bladder and the sigmoid, the scatter of the IQR of the D_{2cm^3} for Gy_{EQD2} is higher than for the rectum and the bowel. This suggests that these organs are sensitive to deviations caused by the AI-based reconstruction of the applicator. Of course, due to its proximity to the applicator with the steep dose gradient, the dose level of the sigmoid is also higher than that of the bowel.

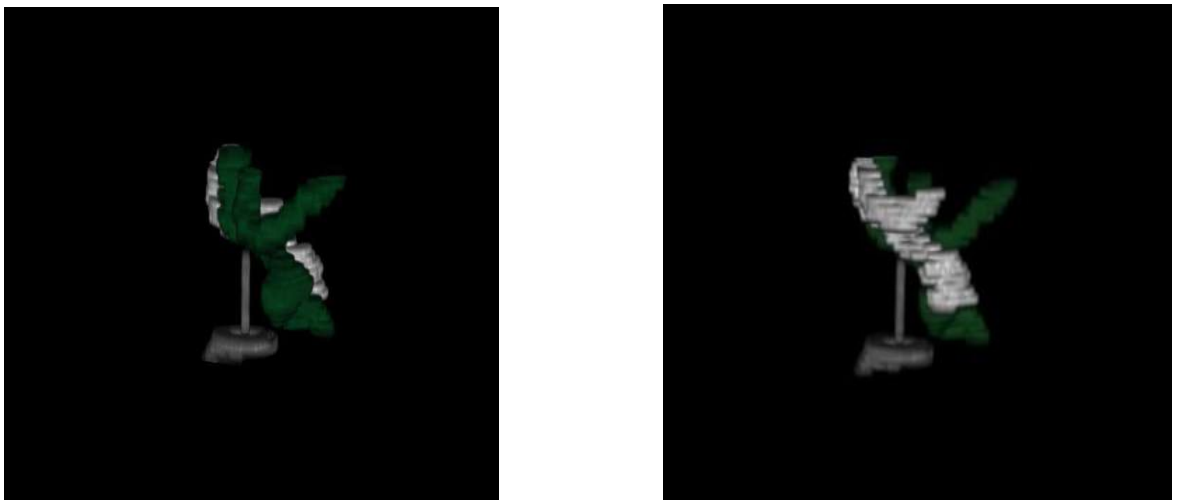

Fig. 27 Case EVIMR0006: Sigmoid position in white EVIMR0006 clin and green EVIMR0006 pre to the applicator after registration for (I) left: the AI-based reconstruction and (II) right: the AS-based reconstruction. In the left image, Sigmoid is closer to the applicator, resulting in a higher dose. - created in Hero

A comparison of the dose-related interfraction variations of the AS-based registration with the AI-based registration shows that for all cases considered, the scatter of the difference in interfraction variations (IQR) is higher for the AI-based than for the AS-based method. Although the results are similar on average, the scatter of the calculated values is much higher for AI-based registration. This result is to be expected based on the results of the work of Ecker et al [11]. It can be seen that the AI-based reconstruction of the applicator and the subsequent registration is still less accurate than the AS resulting from the reconstruction of the applicator in the TPS. This also has a dosimetric influence on the interfraction variation and the results of the AS-based method differ from those of the manual method. The large mean deviation of the AI-based reconstruction for the sigmoid in all plots can be attributed to the shift caused by the registration towards the applicator for case EVIMR0006 (see Fig. 27). The shift of the entire organ towards an area irradiated with a steeper dose gradient, i.e. closer to the implant, changes the D_{2cm^3} considerably. This results in outliers as described in Chapter 4.3 (e.g. Fig. 22 inter_post$_{AI}$= -20.83 Gy_{EQD2}). However, these very high dose values are extreme in this case and show that there are cases where registration based on AI does not work well yet. Nevertheless, in most cases the AI gives good enough results for a rough estimation of the interfraction variations. The results of our study also show that different considerations must be made for each OAR. For example, the results obtained here for the AI variations for the sigmoid and the bladder are quite different from those based on the AS. In contrast, they are comparable for the AS for rectum and bowel.

For the bladder, the results show a large dosimetric scatter when using the AI. This deviation is clearly higher than that of the registration based on the AS. The bladder runs along almost the entire anterior length of the applicator (both tandem and ring). As a result, it receives an average D_{2cm^3} absorbed dose of 5.8 Gy [4] per fraction. Due to this high average dose, small shifts and changes between applicators and bladder have a very large influence on the D_{2cm^3} in EQD2. This effect is particularly pronounced in the bladder, as the bladder is exposed to a high dose and the uncertainty of the absorbed dose has a greater influence on the change in EQD2 at high doses and a lesser influence at low doses. In addition, inter-fraction variations or registration deviations have a large dosimetric impact. For the cases considered here, the registration inaccuracy of the AI is a critical factor. In addition, the dose deviations compared to the manual method are too high to provide useful estimates of the dosimetric interfraction variations. In some cases, however, the AI-based registration is still accurate enough to provide a trend. This trend can be used to further investigate individual cases of high dosimetric deviation.

The sigmoid showed very large deviations. In these cases, the D_{2cm^3} is often divided into several sub volumes, so that these can naturally change considerably with shifts. Although the dose gradient in these cases is much lower than in the bladder, the different D_{2cm^3} spots can change substantially. An additional complication for the analysis is that it is not possible to tell whether the same voxels are observed with the different methods due to the D_{2cm^3} splitting.

This means that the AI is not accurate enough to predict inter- and intrafraction dose variations for the sigmoid.

For the rectum, however, these results suggest that the deviations of the dosimetric interfraction variations of AI are quite similar to those of AS. Moreover, they do not vary very much. The algorithm tends to slightly overestimate the values obtained in TPS. However, the values only vary by about ±10%, which would be acceptable as an uncertainty, since the random SD in the rectum is ±21.7% [10]. In the rectum, D_{2cm^3} is often at a contiguous volume and is mainly influenced by the ring dose. As a result, the rectum remains stable for interfraction variation for all registration methods studied.

The bowel showed similar patterns of variation in the interfraction variations observed for both AI and AS. The results showed that the bowel is subject to quite strong random interfraction variations. In comparison, the methods are shown to be equally robust to these. Of course, the dose level for the bowel is also considerably lower than, for example, for the sigmoid or even the bladder, which means that interfraction and intrafraction variations often have a lower dosimetric impact.

Since the same tool is used here to generate the AS and the same neural network is used for the AI-based prediction as in Ecker et al. [11], the results of Ecker et al. can be used for the Mean Distance Error (MDE) deviations. The similar DICE coefficient confirms this. Therefore, an MDE of 0.7 ±0.5 mm is assumed for the AS and an MDE of 2.7 ±1.4 mm for the AI. To answer the question “At what MDE is an algorithm accurate enough to make a good prediction?", the available values for the AS must be used as a guide. From the results of the dosimetric inter- and intrafraction variations in this work, a tool should have an MDE close to that of the AS. It can therefore be concluded that a tool in the range of the MDE of the AS and a mean registration error of <1mm, does not produce significant dosimetric errors (on average). For individual organs such as the bowel, a greater margin of tolerance is acceptable as the AI also achieves similar results to the AS with an MDE of 2.7 ±1.4 mm. To make a good prediction for all organs, the deviation should be close to 0.7 ±0.5 mm.

In summary, we found that the algorithm performed inferiorly to the manual method over the full range of interfraction variations. This was expected based on the results of Ecker et al [11]. Nevertheless, it proved to be an effective means of estimating the interfraction variations that occur particularly for rectum and bowel. An algorithm for good dosimetric prediction of inter- and intrafraction variations of all organs should have a mean registration error of <1mm.

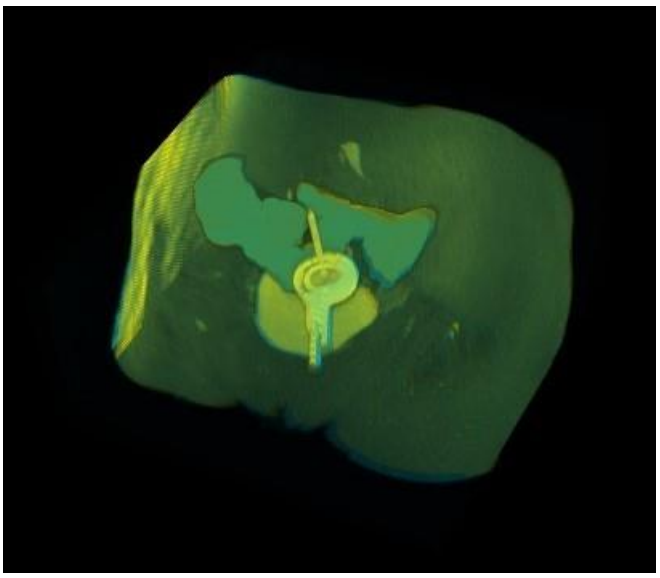

Fig. 28 Registration error EVIMR0005 pre between AS-based registration (yellow) & AI-based registration (turquoise). The image is rotated slightly to the right and shifted downwards due to the AI-based registration. - created in Hero

5.3.1 OUTLOOK

To improve the detection of interfraction variation based on AI, a better resolution of MR would be a reasonable option. The 2D MR used in this study had a slice thickness of 5mm between image sequences, which results in a limited cranio-caudal image resolution when only transversal MRI series are included in the automatic registration. This also increases the impact of differences in ROI-interpolation by different programs on DVH calculations. The new MR scanner recently installed at the Department of Radiation Oncology of the AKH /MUW has a much lower slice thickness of only 3mm. In addition, 3D sequencing is another method to be considered to provide significantly better 3D resolution. Training with these new image datasets would create a more accurate network and thus enable more reliable registration.

Based on the Hero script created as part of this work, future assessments can be repeated on the same basis. This should also be done for a more valid assessment of those cases where the presented AI proves to be an effective means of assessing interfraction variation. The nine cases examined in this paper are limited to making a general statement about the functionality of AI for interfraction variation detection. Therefore, this study should be replicated with a more accurate AI for higher resolution MR images and a larger data set.

A APPENDIX

TNM	FIGO	Definition
Tx		Primary tumor cannot be assessed
T0		No evidence of primary tumor
Tis		Preinvasive carcinoma
T1	I	Cervical carcinoma confined to cervix (extension to corpus should be disregarded)
T1a	IA	Invasive carcinoma diagnosed only by microscopy, with maximum depth of invasion < 5 mm.
T1a1	IA1	Measured stromal invasion 3 mm or less in depth.
T1a2	IA2	Measured stromal invasion more than ≥ 3 mm and < 5 mm in depth.
T1b	IB	Clinically visible lesion confined to the cervix or microscopic lesion greater than IA2
T1b1	IB1	Invasive carcinoma ≥ 5 mm mm depth of stromal invasion, and < 2 cm in greatest dimension
T1b2	IB2	Invasive carcinoma with greatest dimension of ≥ 2 cm and < 4 cm
	IB3	Invasive carcinoma with greatest dimension of > 4 cm
T2	II	The carcinoma invades beyond the uterus, but has not extended into the lower third of the vagina or to the pelvic wall
T2a	IIA	Involvement limited to the upper two-thirds of the vagina without parametrial invasion
T2a1	IIA1	Invasive carcinoma with greatest dimension of < 4 cm
T2a2	IIA2	Invasive carcinoma with greatest dimension of ≥ 4cm
T2b	IIB	With parametrial involvement but not up to the pelvic wall
T3	III	The carcinoma involves the lower third of the vagina and/or extends to the pelvic wall and/or causes hydronephrosis or nonfunctioning kidney and/or involves pelvic and/or para-aortic lymph nodes
T3a	IIIA	The carcinoma involves the lower third of the vagina, with no extension to the pelvic wall
T3b	IIIB	Extension to the pelvic wall and/or hydronephrosis or nonfunctioning kidney (unless known to be due to another cause)
N	IIIC	Involvement of pelvic and/or para-aortic lymph nodes, irrespective of tumor size and extent (with r and p notations)
T4	IV	The carcinoma has extended beyond the true pelvis or has involved (biopsy proven) the mucosa of the bladder or rectum (the presence of bullous edema is not sufficient to classify a case as Stage IV)
	IVA	Spread to adjacent pelvic organs
M1	IVB	Spread to distant organs

Table 5 TNM (8th Edition) and FIGO (2018) Classification of cervical cancer [17]

ROI	Patient	F1	Volume[cm³]	D2 [Gy]	EQD2 [Gy]	D0.1 [Gy]	EQD0.1 [Gy]	F2_pre	Volume[cm³]	D2 [Gy]	EQD2 [Gy]	D0.1 [Gy]	EQD0.1 [Gy]	F2_post	Volume[cm³]	D2 [Gy]	EQD2 [Gy]	D0.1 [Gy]	EQD0.1 [Gy]
bladder	EVIMR0001		116,95	4,46	6,64	5,77	10,13		214,33	5,82	10,28	7,63	16,21		132,78	4,72	7,29	6,05	10,95
	EVIMR0003		100,16	6,81	13,35	8,50	19,56		146,31	6,95	13,83	8,62	20,01		178,23	6,96	13,86	8,56	19,79
	EVIMR0004		102,34	5,32	8,85	7,82	16,91		157,57	5,74	10,04	8,24	18,54		236,08	6,72	13,06	9,55	23,95
	EVIMR0005		110,36	5,39	9,05	7,46	15,61		107,46	5,91	10,54	8,51	19,60		121,26	6,02	10,87	7,80	16,84
	EVIMR0006		160,89	5,10	8,25	5,85	10,36		277,86	6,17	11,31	7,38	15,32		569,49	7,38	15,32	8,92	21,24
	EVIMR0007		92,76	4,87	7,68	6,20	11,39		138,65	5,69	9,87	7,25	14,85		141,30	5,80	10,22	7,37	15,29
	EVIMR0008		293,03	4,70	7,25	6,36	11,89		229,20	4,76	7,39	6,11	11,14		149,97	3,84	5,26	5,28	8,74
	EVIMR0009		160,86	4,81	7,51	5,73	10,01		161,28	4,53	6,81	5,35	8,94		215,14	4,85	7,61	6,30	11,71
	EVIMR0010		109,57	5,54	9,47	6,50	12,36		125,96	6,42	12,10	8,36	18,99		157,77	6,42	12,10	8,24	18,53
rectum	EVIMR0001		66,88	1,58	1,45	2,03	2,05		47,42	1,88	1,84	2,46	2,68		54,93	1,83	1,76	2,36	2,53
	EVIMR0003		75,73	4,38	6,47	5,54	9,47		47,51	4,38	6,47	5,75	10,07		51,57	4,40	6,50	5,81	10,23
	EVIMR0004		44,38	2,09	2,12	2,59	2,90		30,85	1,99	1,99	2,59	2,90		37,42	1,95	1,93	2,48	2,72
	EVIMR0005		42,95	2,77	3,19	3,69	4,94		27,93	1,98	1,97	2,52	2,77		25,24	2,17	2,24	2,71	3,09
	EVIMR0006		30,03	4,07	5,76	5,26	8,69		18,71	3,30	4,17	4,46	6,66		18,30	3,46	4,48	4,59	6,97
	EVIMR0007		44,57	3,60	4,75	4,64	7,08		79,83	3,86	5,30	4,89	7,72		36,15	3,41	4,37	4,24	6,14
	EVIMR0008		29,16	2,07	2,10	3,01	3,62		58,59	3,47	4,49	5,03	8,08		48,18	3,73	5,02	5,75	10,06
	EVIMR0009		54,52	3,26	4,08	4,16	5,97		46,27	3,24	4,04	4,03	5,66		49,39	3,38	4,31	4,27	6,21
	EVIMR0010		56,24	2,49	2,74	3,25	4,07		13,05	3,08	3,75	4,46	6,65				0,00		0,00
sigmoid	EVIMR0001		62,51	2,67	3,03	3,38	4,31		45,31	3,02	3,64	3,97	5,53		40,64	3,00	3,59	4,27	6,20
	EVIMR0003		74,13	2,93	3,48	3,91	5,39		54,49	1,63	1,51	2,07	2,10		76,48	1,80	1,72	2,33	2,49
	EVIMR0004		81,27	3,98	5,56	5,19	8,49		112,14	3,36	4,27	4,53	6,81		94,44	3,07	3,73	4,12	5,87
	EVIMR0005		51,02	3,85	5,28	5,01	8,03		81,63	4,75	7,36	7,40	15,38		83,33	4,53	6,83	5,95	10,66
	EVIMR0006		55,10	3,73	5,01	5,27	8,72		84,79	5,59	9,60	7,22	14,76		87,26	5,68	9,87	7,95	17,42
	EVIMR0007		53,96	2,51	2,77	3,09	3,77		82,46	2,91	3,43	3,88	5,35		101,19	3,50	4,55	4,96	7,89
	EVIMR0008		84,57	3,54	4,62	4,83	7,55		119,87	3,91	5,41	5,81	10,24		136,49	3,78	5,12	5,72	9,98
	EVIMR0009		110,08	3,67	4,89	5,30	8,78		91,19	3,64	4,83	5,44	9,18		109,68	3,80	5,17	5,28	8,75
	EVIMR0010		135,45	4,37	6,43	5,15	8,39		147,82	4,62	7,04	5,84	10,33		200,10	4,88	7,68	6,37	11,94
bowel	EVIMR0001		218,97	4,47	6,69	6,02	10,87		291,72	4,27	6,21	6,65	12,83		295,98	4,32	6,32	6,17	11,32
	EVIMR0003		291,88	3,15	3,87	4,18	6,01		432,74	2,92	3,45	3,56	4,67		372,35	2,61	2,93	3,21	3,99
	EVIMR0004		7,39	0,46	0,32	0,77	0,58		47,90	0,81	0,61	1,10	0,91		19,89	0,67	0,49	0,97	0,77
	EVIMR0005		16,72	1,15	0,95	1,77	1,69		146,43	4,11	5,84	7,57	16,02		90,33	2,37	2,55	3,82	5,21
	EVIMR0006		26,60	0,46	0,32	0,77	0,58		50,22	0,73	0,55	1,04	0,84		72,28	0,60	0,43	0,91	0,71
	EVIMR0007		231,20	1,34	1,16	1,64	1,52		36,48	1,12	0,92	1,44	1,28		43,38	1,13	0,93	1,44	1,28
	EVIMR0008		387,95	3,35	4,26	4,90	7,75		326,13	3,86	5,29	4,96	7,90		428,79	5,09	8,25	7,41	15,44
	EVIMR0009		25,79	0,83	0,63	1,14	0,95		42,09	1,17	0,98	1,53	1,39		29,37	0,91	0,71	1,22	1,03
	EVIMR0010		144,91	2,35	2,51	3,22	4,01		180,89	2,78	3,21	3,73	5,02		166,68	1,68	1,57	2,15	2,21

Table 6 DVH data of the applicator structure based registration of the planning MR with the two MR of the second fraction.

ROI	Patient	F1	Volume[cm³]	D2 [Gy]	EQD2 [Gy]	D0.1 [Gy]	EQD0.1 [Gy]	F2_pre	Volume[cm³]	D2 [Gy]	EQD2 [Gy]	D0.1 [Gy]	EQD0.1 [Gy]	F2_post	Volume[cm³]	D2 [Gy]	EQD2 [Gy]	D0.1 [Gy]	EQD0.1 [Gy]
bladder	EVIMR0001		117,86	4,26	6,18	5,65	9,78		217,27	5,60	9,62	8,10	18,00		137,54	4,69	7,21	6,22	11,48
	EVIMR0003		101,06	6,66	12,86	8,41	19,21		148,19	7,00	14,00	14,35	49,79		179,80	6,92	13,73	9,36	23,15
	EVIMR0004		103,37	5,10	8,25	7,90	17,23		159,89	5,73	10,00	8,86	21,01		238,07	6,77	13,23	10,00	25,99
	EVIMR0005		111,14	5,24	8,62	7,42	15,47		109,90	6,10	11,12	9,12	22,11		122,66	6,12	11,17	9,33	23,01
	EVIMR0006		163,12	4,75	7,35	5,55	9,50		279,87	5,82	10,25	7,23	14,78		573,22	6,86	13,52	8,56	19,80
	EVIMR0007		94,31	4,75	7,36	6,28	11,65		141,40	5,49	9,32	7,42	15,47		144,32	5,61	9,65	7,44	15,55
	EVIMR0008		295,03	4,53	6,82	6,35	11,89		233,61	4,53	6,82	6,06	10,99		152,99	3,78	5,12	5,23	8,61
	EVIMR0009		163,57	4,60	6,99	5,51	9,38		162,93	4,25	6,17	5,13	8,35		217,11	4,48	6,70	5,84	10,33
	EVIMR0010		110,40	5,33	8,88	6,31	11,75		127,04	6,27	11,63	8,85	20,95		159,14	6,14	11,22	8,42	19,24
rectum	EVIMR0001		67,81	1,33	1,15	1,73	1,64		47,61	1,67	1,56	2,26	2,38		55,12	1,61	1,49	2,33	2,49
	EVIMR0003		76,17	4,16	5,96	5,34	8,91		46,86	4,16	5,96	5,61	9,67		47,85	4,13	5,90	5,51	9,37
	EVIMR0004		44,93	1,84	1,79	1,84	1,79		32,60	1,74	1,64	2,59	2,89		39,78	1,72	1,62	2,57	2,87
	EVIMR0005		43,42	2,50	2,75	3,44	4,42		28,90	1,73	1,64	2,46	2,69		26,85	1,90	1,87	2,72	3,11
	EVIMR0006		30,26	3,91	5,40	5,18	8,47		20,03	3,22	4,00	4,96	7,88		19,53	3,41	4,38	5,09	8,23
	EVIMR0007		44,89	3,34	4,23	4,44	6,61		75,20	3,69	4,94	4,90	7,74		31,88	3,24	4,04	4,57	6,93
	EVIMR0008		29,53	1,84	1,78	2,73	3,13		49,16	3,27	4,10	5,53	9,43		37,78	3,52	4,58	5,90	10,52
	EVIMR0009		55,07	3,03	3,66	3,94	5,47		47,38	3,05	3,70	4,04	5,69		49,74	3,20	3,97	4,20	6,04
	EVIMR0010		57,87	2,26	2,38	3,00	3,60		13,58	2,92	3,46	4,47	6,67				0,00		0,00
sigmoid	EVIMR0001		65,56	2,45	2,67	2,45	2,67		49,86	2,91	3,44	4,08	5,77		44,09	2,71	3,09	4,12	5,86
	EVIMR0003		78,11	2,72	3,11	3,72	5,00		56,28	1,85	1,79	1,35	1,17		82,23	1,61	1,48	2,24	2,35
	EVIMR0004		86,79	3,76	5,09	3,76	5,09		109,49	3,28	4,12	4,64	7,08		90,14	2,94	3,49	4,10	5,82
	EVIMR0005		54,56	3,67	4,89	4,90	7,75		85,86	4,70	7,24	8,50	19,53		68,32	4,19	6,03	6,93	13,77
	EVIMR0006		58,82	3,55	4,64	5,23	8,61		87,52	5,45	9,21	7,29	15,01		80,02	5,39	9,04	7,85	17,05
	EVIMR0007		60,53	2,89	3,40	2,32	2,47		85,83	2,73	3,13	3,87	5,32		105,69	3,36	4,27	5,59	9,59
	EVIMR0008		90,88	3,39	4,33	4,95	7,86		124,21	3,54	4,62	5,46	9,24		145,36	3,43	4,42	5,25	8,65
	EVIMR0009		115,46	3,50	4,54	5,22	8,58		94,45	3,62	4,80	5,49	9,33		114,43	3,73	5,02	5,34	8,91
	EVIMR0010		139,87	4,15	5,94	4,95	7,86		153,80	4,46	6,66	5,74	10,03		205,27	4,74	7,34	6,38	11,96
bowel	EVIMR0001		229,43	4,32	6,33	4,32	6,33		287,32	4,38	6,47	7,01	14,05		294,04	4,15	5,94	6,50	12,37
	EVIMR0003		295,29	4,36	6,42	2,65	2,99		336,41	2,65	2,99	3,65	4,86		344,91	2,53	2,79	3,53	4,61
	EVIMR0004		7,61	0,00	0,00	0,45	0,31		32,29	0,59	0,43	0,75	0,56		17,06	0,44	0,30	0,71	0,52
	EVIMR0005		18,75	0,89	0,69	1,62	1,49		134,39	4,05	5,72	8,26	18,62		89,75	2,23	2,33	3,88	5,34
	EVIMR0006		25,39	0,00	0,00	0,00	0,00		49,79	0,27	0,18	0,49	0,34		38,98	0,00	0,00	0,00	0,00
	EVIMR0007		233,74	0,99	0,79	1,24	1,05		37,93	0,89	0,69	1,16	0,96		45,60	0,90	0,70	1,26	1,08
	EVIMR0008		398,73	3,20	3,96	5,15	8,40		335,44	3,73	5,03	5,13	8,34		435,86	5,20	8,53	7,85	17,04
	EVIMR0009		28,66	0,55	0,39	0,75	0,56		37,48	0,78	0,59	1,25	1,06		26,92	0,30	0,19	0,87	0,67
	EVIMR0010		152,19	2,10	2,14	3,15	3,88		191,90	2,58	2,89	3,73	5,03		171,12	1,40	1,23	2,00	2,00

Table 7 DVH data of the manual registration of the planning MR with the two MR of the second fraction.

ROI	Patient	F1	Volume[cm³]	D2 [Gy]	EQD2 [Gy]	D0.1 [Gy]	EQD0.1 [Gy]	F2_pre	Volume[cm³]	D2 [Gy]	EQD2 [Gy]	D0.1 [Gy]	EQD0.1 [Gy]	F2_post	Volume[cm³]	D2 [Gy]	EQD2 [Gy]	D0.1 [Gy]	EQD0.1 [Gy]
Bladder	EVIMR0001		117,86	4,26	6,18	5,65	9,78		217,11	6,18	11,35	9,07	21,89		137,54	5,68	8,27	6,22	11,48
	EVIMR0003		101,06	6,66	12,86	8,41	19,21		148,19	7,11	14,38	14,14	48,44		179,80	7,05	14,18	10,68	29,20
	EVIMR0004		103,37	5,10	8,25	7,90	17,23		159,88	6,18	11,34	10,08	26,36		238,08	5,96	10,68	8,85	20,95
	EVIMR0005		111,14	5,24	8,62	7,42	15,47		109,90	6,17	11,31	9,25	22,67		122,66	5,87	10,43	8,90	21,17
	EVIMR0006		163,12	4,75	7,35	5,55	9,50		279,96	5,68	9,86	7,48	15,68		568,58	6,12	11,17	8,68	20,26
	EVIMR0007		94,31	4,75	7,36	6,28	11,65		141,40	4,28	6,22	5,42	9,11		144,32	5,64	9,75	7,30	15,04
	EVIMR0008		295,03	4,53	6,82	6,35	11,89		233,72	4,87	7,67	6,42	12,11		153,03	3,59	4,72	5,32	8,85
	EVIMR0009		163,57	4,60	6,99	5,51	9,38		162,93	4,16	5,96	4,82	7,54		217,11	4,52	6,81	5,60	9,62
	EVIMR0010		110,40	5,33	8,88	6,31	11,75		127,03	6,97	13,91	9,58	24,09		159,16	7,73	16,58	11,13	31,45
rectum	EVIMR0001		67,81	1,33	1,15	1,73	1,64		49,33	1,55	1,41	2,18	2,26		55,24	1,48	1,32	2,17	2,24
	EVIMR0003		76,17	4,16	5,96	5,34	8,91		46,73	4,12	5,88	5,50	9,35		47,46	4,11	5,84	5,45	9,22
	EVIMR0004		44,93	1,84	1,79	1,84	1,79		31,99	1,67	1,56	2,45	2,67		38,08	1,91	1,88	2,59	2,90
	EVIMR0005		43,42	2,50	2,75	3,44	4,42		28,98	1,84	1,78	2,69	3,06		27,04	1,93	1,90	2,73	3,13
	EVIMR0006		30,26	3,91	5,40	5,18	8,47		20,11	3,49	4,54	4,94	7,84		19,31	3,94	5,48	5,46	9,24
	EVIMR0007		44,89	3,34	4,23	4,44	6,61		74,47	4,72	7,28	6,48	12,28		31,85	3,20	3,96	4,46	6,65
	EVIMR0008		29,53	1,84	1,78	2,73	3,13		47,99	3,00	3,60	4,52	6,81		33,04	3,25	4,06	5,59	9,60
	EVIMR0009		55,07	3,03	3,66	3,94	5,47		46,65	2,90	3,43	3,65	4,85		49,57	3,05	3,69	3,89	5,35
	EVIMR0010		57,87	2,26	2,38	3,00	3,60		13,48	2,10	2,14	2,95	3,51				0,00		0,00
sigmoid	EVIMR0001		65,56	2,45	2,67	2,45	2,67		49,85	2,78	3,21	3,87	5,33		44,12	2,33	2,48	3,37	4,30
	EVIMR0003		78,11	2,72	3,11	3,72	5,00		56,43	1,84	1,78	1,35	1,17		81,95	1,58	1,44	2,16	2,24
	EVIMR0004		86,79	3,76	5,09	3,76	5,09		110,07	3,32	4,20	4,72	7,28		90,33	3,36	4,28	4,88	7,69
	EVIMR0005		54,56	3,67	4,89	4,90	7,75		85,86	4,34	6,36	7,62	16,18		68,33	4,46	6,65	8,11	18,03
	EVIMR0006		58,82	3,55	4,64	5,23	8,61		87,82	7,33	15,16	11,73	34,55		80,86	10,90	30,32	28,05	174,21
	EVIMR0007		60,53	2,89	3,40	2,32	2,47		86,69	3,53	4,61	5,48	9,30		105,70	3,41	4,37	5,70	9,91
	EVIMR0008		90,88	3,39	4,33	4,95	7,86		124,21	3,47	4,49	5,24	8,63		145,36	3,96	5,50	6,83	13,43
	EVIMR0009		115,46	3,50	4,54	5,22	8,58		95,44	3,55	4,65	5,24	8,65		114,95	3,57	4,68	4,95	7,87
	EVIMR0010		139,87	4,15	5,94	4,95	7,86		153,92	4,61	7,01	5,95	10,64		205,48	4,08	5,77	5,17	8,43
bowel	EVIMR0001		229,43	4,32	6,33	4,32	6,33		297,69	4,47	6,68	7,13	14,43		301,78	3,96	5,51	5,95	10,66
	EVIMR0003		295,29	4,36	6,42	2,65	2,99		338,80	2,70	3,08	3,70	4,95		336,02	2,51	2,77	3,48	4,50
	EVIMR0004		7,61	0,00	0,00	0,45	0,31		36,13	0,63	0,46	0,87	0,67		16,99	0,45	0,31	0,72	0,53
	EVIMR0005		18,75	0,89	0,69	1,62	1,49		130,61	4,26	6,18	9,50	23,76		89,39	2,19	2,28	3,85	5,28
	EVIMR0006		25,39	0,00	0,00	0,00	0,00		51,96	0,00	0,00	0,00	0,00		51,40	0,00	0,00	0,00	0,00
	EVIMR0007		233,74	0,99	0,79	1,24	1,05		38,11	0,95	0,75	1,24	1,06		45,64	0,92	0,72	1,27	1,08
	EVIMR0008		398,73	3,20	3,96	5,15	8,40		336,87	3,72	5,01	4,93	7,81		433,48	5,48	9,30	7,77	16,72
	EVIMR0009		28,66	0,55	0,39	0,75	0,56		38,82	0,96	0,76	1,43	1,27		27,79	0,62	0,45	0,95	0,75
	EVIMR0010		152,19	2,10	2,14	3,15	3,88		192,20	2,16	2,23	3,07	3,72		172,51	1,24	1,06	1,69	1,59

Table 8 DVH data of the neural network based registration of the planning MR with the two MR of the second fraction.

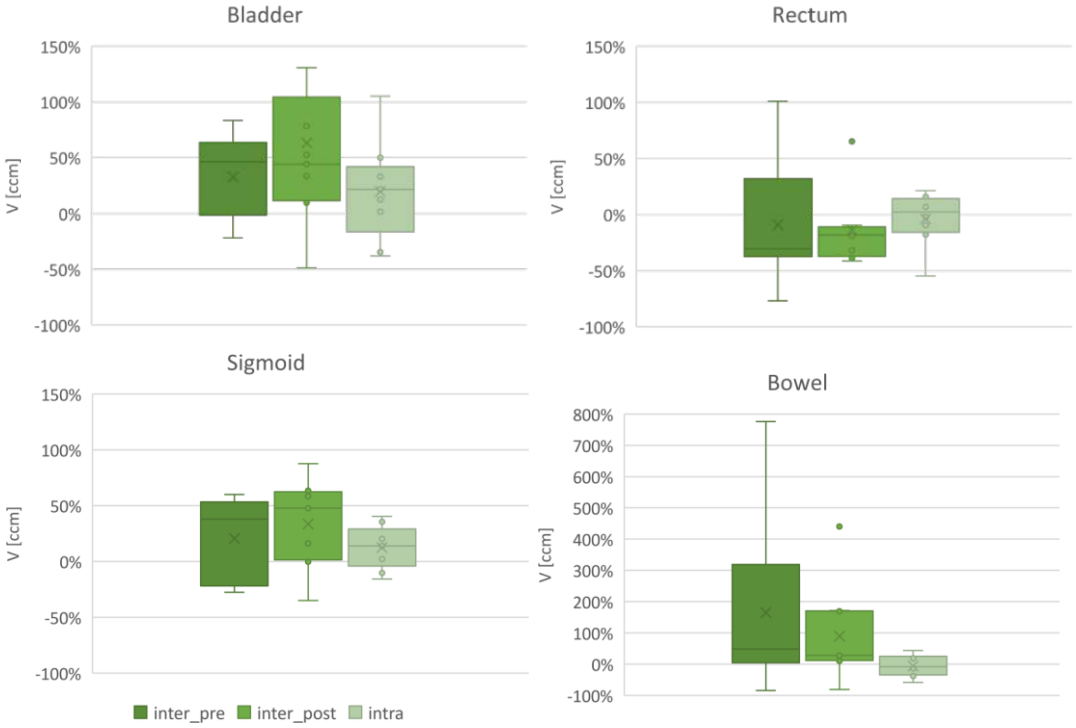

Fig. 29 volume difference of the manual registration in %

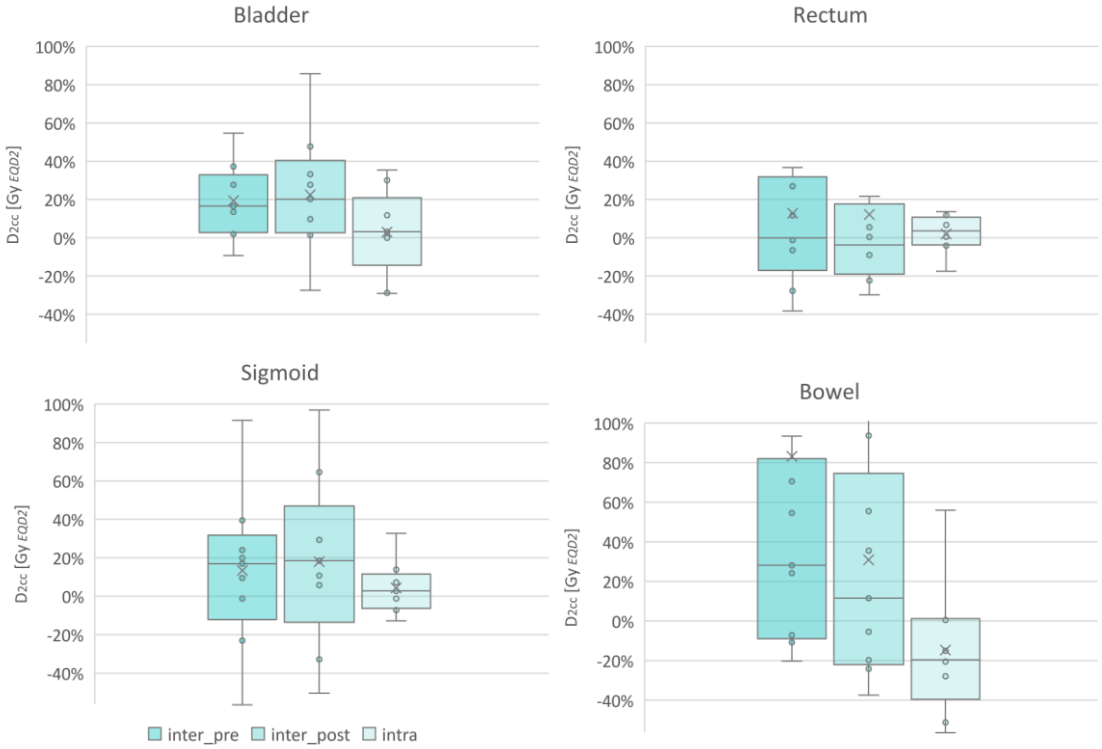

Fig. 30 inter- and intrafraction variation EQD2 of the manual registration in %

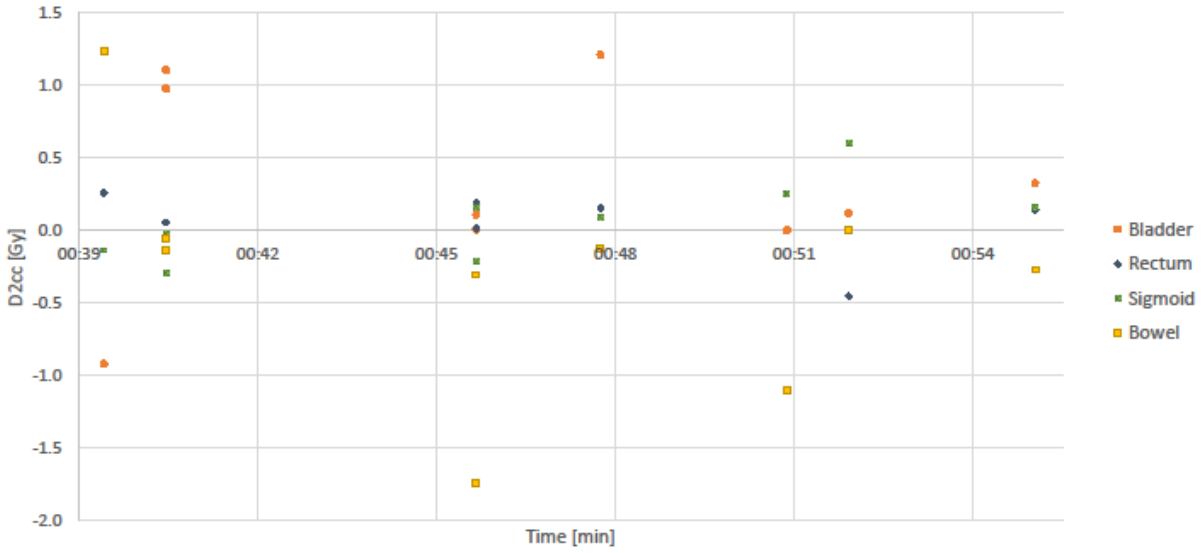

Fig. 31 Intrafraction variation dose to time ratio

p-value

OAR	inter_pre		inter_post		intra	
	GY	GY_{EQD2}	GY	GY_{EQD2}	GY	GY_{EQD2}
bladder	0.32	0.26	0.37	0.37	0.50	0.47
rectum	0.49	0.42	0.43	0.42	0.30	0.27
sigmoid	0.16	0.17	0.18	0.17	0.22	0.18
bowel	0.36	0.35	0.33	0.36	0.48	0.49

Table 9 One-Sided p-value from paired samples t-test with dependent samples for the organs bladder, rectum, sigmoid colon, and bowel.

B REFERENCES

[1] H. Sung *et al.*, “Global Cancer Statistics 2020: GLOBOCAN Estimates of Incidence and Mortality Worldwide for 36 Cancers in 185 Countries,” *CA. Cancer J. Clin.*, vol. 71, no. 3, pp. 209–249, May 2021, doi: 10.3322/caac.21660.

[2] E. L. Franco, E. Duarte-Franco, and A. Ferenczy, “Cervical cancer: epidemiology, prevention and the role of human papillomavirus infection,” *Can. Med. Assoc. J.*, vol. 164, no. 7, p. 1017, Apr. 2001.

[3] P. A. Cohen, A. Jhingran, A. Oaknin, and L. Denny, “Cervical cancer,” *The Lancet*, vol. 393, no. 10167, pp. 169–182, Jan. 2019, doi: 10.1016/S0140-6736(18)32470-X.

[4] Pötter *et al.*, “ICRU Report No.89 - Prescribing, recording, and reporting brachytherapy for cancer of the cervix,” *J. ICRU*, vol. 13, no. 1–2, p. NP.2-NP, Apr. 2013, doi: 10.1093/jicru/ndw028.

[5] R. Pötter *et al.*, “The EMBRACE II study: The outcome and prospect of two decades of evolution within the GEC-ESTRO GYN working group and the EMBRACE studies,” *Clin. Transl. Radiat. Oncol.*, vol. 9, pp. 48–60, Feb. 2018, doi: 10.1016/j.ctro.2018.01.001.

[6] R. Pötter *et al.*, “MRI-guided adaptive brachytherapy in locally advanced cervical cancer (EMBRACE-I): a multicentre prospective cohort study,” *Lancet Oncol.*, vol. 22, no. 4, pp. 538–547, Apr. 2021, doi: 10.1016/S1470-2045(20)30753-1.

[7] A. Sturdza *et al.*, “Image guided brachytherapy in locally advanced cervical cancer: Improved pelvic control and survival in RetroEMBRACE, a multicenter cohort study,” *Radiother. Oncol. J. Eur. Soc. Ther. Radiol. Oncol.*, vol. 120, no. 3, pp. 428–433, Sep. 2016, doi: 10.1016/j.radonc.2016.03.011.

[8] N. B. K. Jensen *et al.*, “Bowel morbidity following radiochemotherapy and image-guided adaptive brachytherapy for cervical cancer: Physician- and patient reported outcome from the EMBRACE study,” *Radiother. Oncol. J. Eur. Soc. Ther. Radiol. Oncol.*, vol. 127, no. 3, pp. 431–439, Jun. 2018, doi: 10.1016/j.radonc.2018.05.016.

[9] L. Fokdal *et al.*, “Physician assessed and patient reported urinary morbidity after radio-chemotherapy and image guided adaptive brachytherapy for locally advanced cervical cancer,” *Radiother. Oncol. J. Eur. Soc. Ther. Radiol. Oncol.*, vol. 127, no. 3, pp. 423–430, Jun. 2018, doi: 10.1016/j.radonc.2018.05.002.

[10] N. Nesvacil *et al.*, "A multicentre comparison of the dosimetric impact of inter- and intra-fractional anatomical variations in fractionated cervix cancer brachytherapy," *Radiother. Oncol.*, vol. 107, no. 1, pp. 20–25, Apr. 2013, doi: 10.1016/j.radonc.2013.01.012.

[11] S. Ecker *et al.*, "Neural network-assisted automated image registration for MRI-guided adaptive brachytherapy in cervical cancer," *Z. Für Med. Phys.*, p. S0939388922000575, May 2022, doi: 10.1016/j.zemedi.2022.04.002.

[12] L. S. Massad, P. J. DiSaia, W. T. Creasman, R. S. Mannel, D. S. McMeekin, and D. G. Mutch, "1 - Preinvasive Disease of the Cervix," in *Clinical Gynecologic Oncology*, 9th ed., Elsevier, 2018, pp. 1-19.e3.

[13] M. S. Lopez *et al.*, "Cervical cancer prevention and treatment in Latin America," *J. Surg. Oncol.*, vol. 115, no. 5, pp. 615–618, Apr. 2017, doi: 10.1002/jso.24544.

[14] C. Chelimo, T. A. Wouldes, L. D. Cameron, and J. M. Elwood, "Risk factors for and prevention of human papillomaviruses (HPV), genital warts and cervical cancer," *J. Infect.*, vol. 66, no. 3, pp. 207–217, Mar. 2013, doi: 10.1016/j.jinf.2012.10.024.

[15] H. W. Chesson, E. F. Dunne, S. Hariri, and L. E. Markowitz, "The Estimated Lifetime Probability of Acquiring Human Papillomavirus in the United States," *Sex. Transm. Dis.*, vol. 41, no. 11, pp. 660–664, Nov. 2014, doi: 10.1097/OLQ.0000000000000193.

[16] C. A. Johnson, D. James, A. Marzan, and M. Armaos, "Cervical Cancer: An Overview of Pathophysiology and Management," *Semin. Oncol. Nurs.*, vol. 35, no. 2, pp. 166–174, Apr. 2019, doi: 10.1016/j.soncn.2019.02.003.

[17] M. M. Otero-García *et al.*, "Role of MRI in staging and follow-up of endometrial and cervical cancer: pitfalls and mimickers," *Insights Imaging*, vol. 10, no. 1, p. 19, Feb. 2019, doi: 10.1186/s13244-019-0696-8.

[18] M. Arbyn *et al.*, "European Guidelines for Quality Assurance in Cervical Cancer Screening. Second Edition—Summary Document," *Ann. Oncol.*, vol. 21, no. 3, pp. 448–458, Mar. 2010, doi: 10.1093/annonc/mdp471.

[19] N. Popper and C. Rippinger, "Kurzbericht Humane Papillomaviren (HPV) Evaluierung der HPV-Durchimpfungsraten mit einem dynamischen agentenbasierten Simulationsmodell, Version 1.0." Bundesministerium für Soziales, Gesundheit, Pflege und Konsumentenschutz (BMSGPK), Apr. 25, 2023.

[20] C. Haie-Meder, P. Morice, and M. Castiglione, “Cervical cancer: ESMO Clinical Practice Guidelines for diagnosis, treatment and follow-up,” *Ann. Oncol.*, vol. 21, pp. v37–v40, May 2010, doi: 10.1093/annonc/mdq162.

[21] U. Mahantshetty *et al.*, “IBS-GEC ESTRO-ABS recommendations for CT based contouring in image guided adaptive brachytherapy for cervical cancer,” *Radiother. Oncol.*, vol. 160, pp. 273–284, Jul. 2021, doi: 10.1016/j.radonc.2021.05.010.

[22] M. M. Harkenrider, F. Alite, S. R. Silva, and W. Small, “Image-Based Brachytherapy for the Treatment of Cervical Cancer,” *Int. J. Radiat. Oncol. Biol. Phys.*, vol. 92, no. 4, pp. 921–934, Jul. 2015, doi: 10.1016/j.ijrobp.2015.03.010.

[23] D. Baltas, L. Sakelliou, and N. Zamboglou, *The Physics of Modern Brachytherapy for Oncology*. Boca Raton: CRC Press, 2006. doi: 10.1201/9781420012422.

[24] R. Sauer, *Strahlentherapie und Onkologie*, 5th ed. Urban & Fischer in Elsevier, 2009. Accessed: Mar. 07, 2023. [Online]. Available: https://www.facultas.at/item/Strahlentherapie_und_Onkologie/Rolf_Sauer/4757661

[25] W. Y. Song, K. Tanderup, and B. Pieters, “Medical University of Vienna, Vienna, Austria,” in *Emerging Technologies in Brachytherapy*, 1st ed., CRC Press, 2017.

[26] W. Schlegel, C. Karger, and O. Jäkel, *Medizinische Physik Grundlagen – Bildgebung – Therapie – Technik: Grundlagen – Bildgebung – Therapie – Technik*. 2018. doi: 10.1007/978-3-662-54801-1.

[27] T. P. Hellebust *et al.*, “Recommendations from Gynaecological (GYN) GEC-ESTRO Working Group: Considerations and pitfalls in commissioning and applicator reconstruction in 3D image-based treatment planning of cervix cancer brachytherapy,” *Radiother. Oncol.*, vol. 96, no. 2, pp. 153–160, Aug. 2010, doi: 10.1016/j.radonc.2010.06.004.

[28] L. Boldrini, J.-E. Bibault, C. Masciocchi, Y. Shen, and M.-I. Bittner, “Deep Learning: A Review for the Radiation Oncologist,” *Front. Oncol.*, vol. 9, 2019, Accessed: Jun. 05, 2023. [Online]. Available: https://www.frontiersin.org/articles/10.3389/fonc.2019.00977

[29] M. De Brabandere, T. Hellebust, C. Kirisits, F.-A. Siebert, J. Swamidas, and K. Tanderup, “SP-0126 Image registration, Automated segmentation, and Dose Summation,” *Radiother. Oncol.*, vol. 158, pp. S92–S93, May 2021, doi: 10.1016/S0167-8140(21)06514-2.

[30] M. Joiner and A. van der Kogel, Eds., *Basic clinical radiobiology*, 4th ed. London: Hodder Arnold, 2009.

[31] S. M. Bentzen *et al.*, "Bioeffect modeling and equieffective dose concepts in radiation oncology--terminology, quantities and units," *Radiother. Oncol.*, vol. 105, no. 2, pp. 266–268, Nov. 2012, doi: 10.1016/j.radonc.2012.10.006.

[32] R. Pötter *et al.*, "Recommendations from gynaecological (GYN) GEC ESTRO working group (II): Concepts and terms in 3D image-based treatment planning in cervix cancer brachytherapy—3D dose volume parameters and aspects of 3D image-based anatomy, radiation physics, radiobiology," *Radiother. Oncol.*, vol. 78, no. 1, pp. 67–77, Jan. 2006, doi: 10.1016/j.radonc.2005.11.014.

[33] M. Schmid, C. Kirisits, J. Dimopoulos, N. Nesvacil, and R. Pötter, "Local recurrences in cervical cancer patients in the setting of image-guided brachytherapy: A comparison of spatial dose distribution within a matched-pair analysis," *Radiother. Oncol. - RADIOTHER ONCOL*, vol. 99, May 2011, doi: 10.1016/S0167-8140(11)70270-5.

[34] N. Wachter-Gerstner *et al.*, "Bladder and rectum dose defined from MRI based treatment planning for cervix cancer brachytherapy: comparison of dose-volume histograms for organ contours and organ wall, comparison with ICRU rectum and bladder reference point," *Radiother. Oncol. J. Eur. Soc. Ther. Radiol. Oncol.*, vol. 68, no. 3, pp. 269–276, Sep. 2003, doi: 10.1016/s0167-8140(03)00189-0.

[35] M. P. Schmid *et al.*, "Risk Factors for Local Failure Following Chemoradiation and Magnetic Resonance Image-Guided Brachytherapy in Locally Advanced Cervical Cancer: Results From the EMBRACE-I Study," *J. Clin. Oncol. Off. J. Am. Soc. Clin. Oncol.*, vol. 41, no. 10, pp. 1933–1942, Apr. 2023, doi: 10.1200/JCO.22.01096.

[36] C. Kirisits *et al.*, "Accuracy of volume and DVH parameters determined with different brachytherapy treatment planning systems," *Radiother. Oncol. J. Eur. Soc. Ther. Radiol. Oncol.*, vol. 84, no. 3, pp. 290–297, Sep. 2007, doi: 10.1016/j.radonc.2007.06.010.

[37] N. Nesvacil, K. Tanderup, J. C. Lindegaard, R. Pötter, and C. Kirisits, "Can reduction of uncertainties in cervix cancer brachytherapy potentially improve clinical outcome?," *Radiother. Oncol.*, vol. 120, no. 3, pp. 390–396, Sep. 2016, doi: 10.1016/j.radonc.2016.06.008.

[38] C. N. Nomden, A. A. C. de Leeuw, J. M. Roesink, R. J. H. A. Tersteeg, H. Westerveld, and I. M. Jürgenliemk-Schulz, “Intra-fraction uncertainties of MRI guided brachytherapy in patients with cervical cancer,” *Radiother. Oncol.*, vol. 112, no. 2, pp. 217–220, Aug. 2014, doi: 10.1016/j.radonc.2014.08.010.

[39] J. Swamidas, C. Kirisits, M. De Brabandere, T. P. Hellebust, F.-A. Siebert, and K. Tanderup, “Image registration, contour propagation and dose accumulation of external beam and brachytherapy in gynecological radiotherapy,” *Radiother. Oncol.*, vol. 143, pp. 1–11, Feb. 2020, doi: 10.1016/j.radonc.2019.08.023.

[40] K. Tanderup *et al.*, “Evidence-Based Dose Planning Aims and Dose Prescription in Image-Guided Brachytherapy Combined With Radiochemotherapy in Locally Advanced Cervical Cancer,” *Semin. Radiat. Oncol.*, vol. 30, no. 4, pp. 311–327, Oct. 2020, doi: 10.1016/j.semradonc.2020.05.008.

[41] K. Tanderup, N. Nesvacil, R. Pötter, and C. Kirisits, “Uncertainties in image guided adaptive cervix cancer brachytherapy: Impact on planning and prescription,” *Radiother. Oncol.*, vol. 107, no. 1, pp. 1–5, Apr. 2013, doi: 10.1016/j.radonc.2013.02.014.

[42] C. Kirisits *et al.*, “Review of clinical brachytherapy uncertainties: Analysis guidelines of GEC-ESTRO and the AAPM,” *Radiother. Oncol.*, vol. 110, no. 1, pp. 199–212, Jan. 2014, doi: 10.1016/j.radonc.2013.11.002.

[43] S. Lang *et al.*, “Uncertainty analysis for 3D image-based cervix cancer brachytherapy by repetitive MR imaging: assessment of DVH-variations between two HDR fractions within one applicator insertion and their clinical relevance,” *Radiother. Oncol. J. Eur. Soc. Ther. Radiol. Oncol.*, vol. 107, no. 1, pp. 26–31, Apr. 2013, doi: 10.1016/j.radonc.2013.02.015.

[44] K. Tanderup *et al.*, “Consequences of random and systematic reconstruction uncertainties in 3D image based brachytherapy in cervical cancer,” *Radiother. Oncol.*, vol. 89, no. 2, pp. 156–163, Nov. 2008, doi: 10.1016/j.radonc.2008.06.010.

[45] B. Akinrimisi, “Validation of Catalyst HD™ positioning performance using a deformable phantom,” 2019.

[46] S. Klein, M. Staring, K. Murphy, M. A. Viergever, and J. Pluim, “elastix: A Toolbox for Intensity-Based Medical Image Registration,” *IEEE Trans. Med. Imaging*, vol. 29, no. 1, pp. 196–205, Jan. 2010, doi: 10.1109/TMI.2009.2035616.

[47] A. Gerbaulet, R. Pötter, J.-J. Mazeron, H. Meertens, E. Limbergen, and J.-J. Mazeron, *The GEC ESTRO Handbook of Brachytherapy*, 1st ed. ESTRO, 2002.

[48] D. Berger, J. Dimopoulos, R. Pötter, and C. Kirisits, "Direct reconstruction of the Vienna applicator on MR images," *Radiother. Oncol.*, vol. 93, no. 2, pp. 347–351, Nov. 2009, doi: 10.1016/j.radonc.2009.07.002.

[49] A. S. Lundervold and A. Lundervold, "An overview of deep learning in medical imaging focusing on MRI," *Z. Für Med. Phys.*, vol. 29, no. 2, pp. 102–127, May 2019, doi: 10.1016/j.zemedi.2018.11.002.

[50] I. Goodfellow, Y. Bengio, and A. Courville, *Deep Learning*. MIT Press, 2016.

[51] Y. Lecun, L. Bottou, Y. Bengio, and P. Haffner, "Gradient-Based Learning Applied to Document Recognition," *Proc. IEEE*, vol. 86, pp. 2278–2324, Dec. 1998, doi: 10.1109/5.726791.

[52] J. Redmon, S. Divvala, R. Girshick, and A. Farhadi, "You Only Look Once: Unified, Real-Time Object Detection," in *2016 IEEE Conference on Computer Vision and Pattern Recognition (CVPR)*, Jun. 2016, pp. 779–788. doi: 10.1109/CVPR.2016.91.

[53] K. He, X. Zhang, S. Ren, and J. Sun, "Deep Residual Learning for Image Recognition," in *2016 IEEE Conference on Computer Vision and Pattern Recognition (CVPR)*, Jun. 2016, pp. 770–778. doi: 10.1109/CVPR.2016.90.

[54] J. Hu, L. Shen, S. Albanie, G. Sun, and E. Wu, "Squeeze-and-Excitation Networks," *IEEE Trans. Pattern Anal. Mach. Intell.*, vol. 42, no. 8, pp. 2011–2023, Aug. 2020, doi: 10.1109/tpami.2019.2913372.

[55] F. Milletari, N. Navab, and S.-A. Ahmadi, "V-Net: Fully Convolutional Neural Networks for Volumetric Medical Image Segmentation," in *2016 Fourth International Conference on 3D Vision (3DV)*, Oct. 2016, pp. 565–571. doi: 10.1109/3DV.2016.79.

[56] J. Long, E. Shelhamer, and T. Darrell, "Fully convolutional networks for semantic segmentation," in *2015 IEEE Conference on Computer Vision and Pattern Recognition (CVPR)*, Jun. 2015, pp. 3431–3440. doi: 10.1109/CVPR.2015.7298965.

[57] O. Ronneberger, P. Fischer, and T. Brox, "U-Net: Convolutional Networks for Biomedical Image Segmentation," presented at the LNCS, Oct. 2015, pp. 234–241. doi: 10.1007/978-3-319-24574-4_28.

[58] "ITK | Insight Toolkit." Accessed: Apr. 05, 2024. [Online]. Available: https://itk.org/

[59] W. Schroeder, K. Martin, and W. Lorensen, *The Visualization Toolkit, An Object-Oriented Approach To 3D Graphics*. 2006.

[60] A. N. Viswanathan, B. E. Erickson, and J. Rownd, “Image-Based Approaches to Interstitial Brachytherapy,” in *Gynecologic Radiation Therapy*, A. N. Viswanathan, C. Kirisits, B. E. Erickson, and R. Pötter, Eds., Berlin, Heidelberg: Springer Berlin Heidelberg, 2011, pp. 247–259. doi: 10.1007/978-3-540-68958-4_24.